# Controlling the Beam Current of the EU ITER Gyrotron

Goddijn, Michael

*Award date:*
2023


# Controlling the Beam Current of the EU ITER Gyrotron

MSC THESIS

**Student**

| | |
|---|---|
| student: | Michael Goddijn |
| student number: | 1621645 |
| e-mail: | M.Goddijn@student.tue.nl |

**Assessment committee**

| | |
|---|---|
| Chair: | Prof.dr. R.J.E. Jaspers |
| Member 1: | Prof.dr. M.R. de Baar |
| Member 2: | Dr. E. Westerhof |

**Graduation**

| | | |
|---|---|---|
| Program: | M.Sc. Science and Technology of Nuclear Fusion | |
| Supervisor: | Prof.dr. R.J.E. Jaspers | |
| Date of defense: | April 12, 2023 | |
| Study load (ECTS): | 60 | |
| External supervisors: | Dr. S. Alberti, | (EPFL) |
| | Dr. J.-P. Hogge, | (EPFL) |
| | Dr. T. Goodman. | (EPFL) |

Thesis handed in on March 28, 2023

# Abstract

Gyrotrons are essential parts of electron-cyclotron systems, and play a vital role in the development of nuclear fusion as a sustainable energy source. The current of the electron beam in the gyrotron is a key variable that determines the output power. At the moment, no suitable solution is present to maintain a steady beam current and associated output power. Hence, this research discusses the design of a control system that uses the gyrotron's magnetron injection gun to control the beam current of the EU ITER gyrotron.

First, a suitable model of the magnetron injection gun is designed, for which two approaches are investigated. A lumped-element model is considered, based on last year's work of researchers from the Polytechnic University of Milan. Numerous changes are made to the model to increase its potential, but the performance remains unsatisfactory. In addition, a state-space model is designed for low-power pulses: unsuitable for the control system, but the approach serves as a proof-of-concept for future model developments.

Second, using the lumped-element model, a beam-current control system is designed in MATLAB Simulink. The design is focused on tracking a step-shaped reference using feedback and a PI controller. Special attention is paid to the pulse start, where the Nottingham effect causes the beam current to naturally decrease. This effect is counteracted using a temporal feedforward signal. The control system satisfies a set of design constraints in a large part of the operating space, and promises good results for real-world implementation.

# Contents

# Chapter 1: Introduction

## 1.1 Nuclear fusion

It is well known that the worldwide society faces the energy problem [1]. The global energy demand has drastically increased over the past century. It is expected to -at least- double by the year 2100 compared to the current demand.
The increasing energy demand is met by producing more energy. Sadly, the most-used energy sources are still fossil fuels, which emit greenhouse gasses, thereby leading to climate change. In 2019, only between 9.6-18.7% of the global energy amount was produced sustainably [2], depending on if bio-fuel can be considered as a sustainable energy source.
Energy produced by nuclear fusion can form a part of the solution to the energy problem in the later half of the 21$^{\text{st}}$ century. Fusion energy promises a unique combination of four major advantages over other energy sources [3]: it produces no greenhouse-gas emissions, it produces no long-lived radioactive waste, its fuel is abundantly available over the entire planet, and its reactors are inherently safe. As Lopes Cardozo *et al.* [4] put it shortly: "fusion is safe, clean, for all and for ever".

The most-developed fusion technique is *thermonuclear magnetically-confined fusion*. In this technique, the fuel gas is fused by keeping it at a high temperature, in the range of 100-200 million Kelvin. At such high temperatures, the fuel gas is completely ionised, and becomes a plasma. As the plasma's free charges respond to electromagnetic fields, the plasma can be contained in the reactor using a strong magnetic field. To achieve the high target temperature, the plasma can be heated up to a certain level where it achieves *burn*: at this point, sufficient (exothermic!) fusion reactions can take place and their energy is contained long enough, such that the plasma heats itself further to the required target temperature, where the most fusion reactions take place [1].
As one can imagine, special techniques and devices are needed to heat up a fusion plasma. One of the most-important heating techniques is *electron cyclotron heating*.

### 1.1.1 Electron cyclotron heating

The electron cyclotron (EC) heating technique is based on the *wave-particle interaction* between free electrons in the fusion plasma, and electromagnetic (EM) waves that are injected into the plasma [5].

In general, charged particles that are located in a magnetic field will experience a gyrating motion around the magnetic field lines, if the particles have some velocity perpendicular to the magnetic field. This motion is referred to as *cyclotron motion*. The frequency with which the charged particles gyrate is referred to as the *cyclotron frequency*, $f_c$, which is given by [6, p.20]:

$$f_c = \frac{|q|B}{2\pi m} \ \text{[Hz]}, \tag{1.1}$$

with $q$ [C] the particle's charge, $B$ [T] the magnetic field strength, and $m$ [kg] the particle's mass. For an electron, $q = -e$ (the elementary charge), and its cyclotron frequency is thus equal to:

$$f_{ce} = \frac{eB}{2\pi m_e} \approx 28.0 \cdot B \quad [\text{GHz}]. \tag{1.2}$$

When we inject a wave into the plasma, there can be an exchange of energy with the gyrating electrons, if the wave fulfills the resonance condition:

$$f = n f_{ce} + \frac{1}{2\pi} k_{\parallel} v_{\parallel} \quad [\text{Hz}], \quad n \in \mathbb{N}, \tag{1.3}$$

with $f$ the wave frequency, $k_{\parallel}$ [$\text{m}^{-1}$] the angular wave number along the magnetic field, and $v_{\parallel}$ [$\text{m}\cdot\text{s}^{-1}$] the electron velocity along the magnetic field. Clearly, the EC technique uses EM waves at a high frequency, in the order of -at least- tens of GHz. Correspondingly, the wavelength of the injected wave is small.

The EC technique has numerous applications in controlling a fusion experiment. It can be used for [7]:

- central heating of the plasma,
- current drive in the plasma,
- control of magneto-hydrodynamic instabilities and edge-localised modes,
- profile tailoring,
- start-up (break-down, burn-through), ramp-up (current ramp-up, L-to-H-mode transition), and ramp-down (current ramp-down, H-to-L-mode transition).

Due to the small wavelength that is used, the EC technique has the unique advantage over other heating and current-drive techniques that it deposits energy highly locally [1, p.587]. Another advantage of the EC technique is that the output wave can propagate through vacuum. This allows the entire EC system to be located far away from the reactor, which simplifies the reactor design [8]. The EC waves are transported to the plasma using waveguides.

It is safe to conclude: EC heating and current drive is an important technique for the development of fusion [9]. The research into the EC technique is still ongoing. This research concerns both the physics of the wave-particle interaction inside the plasma, and the EC systems outside the plasma.
An EC system consists of a source -which generates the EM waves for the wave-particle interaction- and auxiliary systems, such as transmission lines, high-voltage power supplies (HVPS), launchers, and an EC control system. The source used in the EC system is a device developed specifically for this purpose, called the *gyrotron*, and it is the subject of this thesis.

### 1.1.2 ITER

ITER is the large international fusion experiment that is currently being constructed in the south of France. Its goal is to be the first fusion reactor that shows the feasibility of a burning plasma, and that it is possible to generate more power inside the plasma than that is put into the plasma by auxiliary heating systems. ITER will provide the knowledge to design a demonstration power reactor, which the European Union (EU) plans to construct in the later half of this century. Such a demonstration power reactor will be the first fusion device to deliver net electric energy to the grid. For more general information on ITER, see [11].
ITER's EC system contains 24 gyrotrons, which are going to be used simultaneously to deliver 24 MW of EM wave power, 1 MW each. See Figure 1.1 for an impression of the ITER EC system. By the way

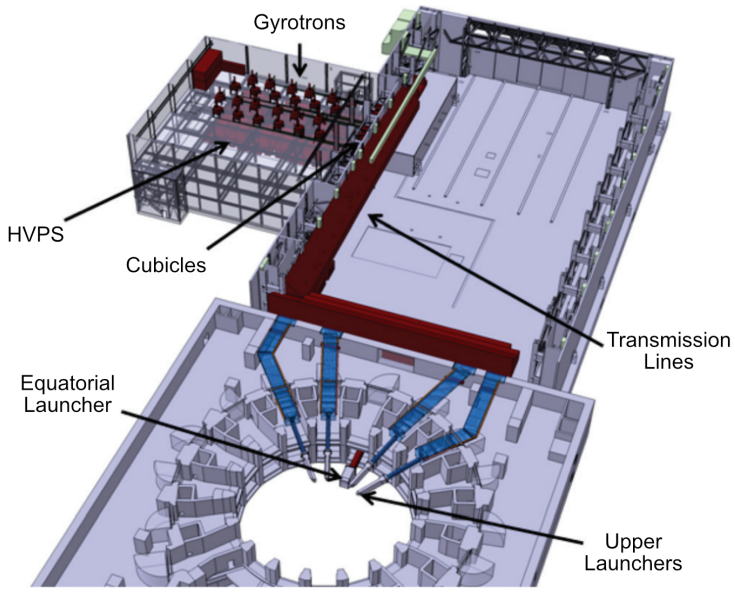


Figure 1.1: Impression of the EC system designed for ITER, showing the separate parts of the system: the gyrotrons, transmission lines, HVPS, and launchers. Figure adapted from [10].

the ITER project is set up, the ITER members (China, EU, India, Japan, Korea, Russia, and the United States) contribute to the project in-kind. The gyrotrons are also developed by different members. In fact, the EU delivers 6 gyrotrons, India delivers 2, Japan delivers 8, and Russia delivers the last 8 [9]. My graduation project specifically concerns the gyrotrons developed by the EU for the ITER project.

For the ITER reactor, the toroidal magnetic field at the center of the plasma is approximately 6T. By Equation (1.2), the cyclotron frequency at the plasma centre is thus 170GHz [12]. The free-space wavelength corresponding to this frequency is $\lambda = 1.76$mm. The gyrotrons are designed to operate at 170GHz, i.e. $n = 1$ in Equation (1.3).

## 1.2 Gyrotrons

Gyrotrons are high-power high-frequency EM wave sources. The gyrotron is a *vacuum electronic device*, whose operation is based on the excitation of a high-harmonic standing wave by an electron beam inside a resonance cavity. In this section, the gyrotron is first compared with other EM wave sources. Then, the operating principle of gyrotrons is discussed. Next, the physics of the electron emission in gyrotrons is explained. Last, it is explained how this electron emission leads to a problem in gyrotrons.

### 1.2.1 Comparison with other sources

Sources capable of delivering EM waves are separated into vacuum electronic devices and solid-state devices. An overview of different types of sources is shown in Figure 1.2. This plot shows the frequency and power range for multiple EM wave sources.
As mentioned, the ITER gyrotrons are designed for an output power of 1MW each at a frequency of 170GHz. From Figure 1.2, it becomes clear that gyrotrons are the only sources capable of operating at 170GHz with 1MW power output.

There is an intuitive reason why traditional (i.e. non-gyrotron) vacuum electronic devices are not suitable for a combined high-frequency and high-power operation. In these devices, the system heating

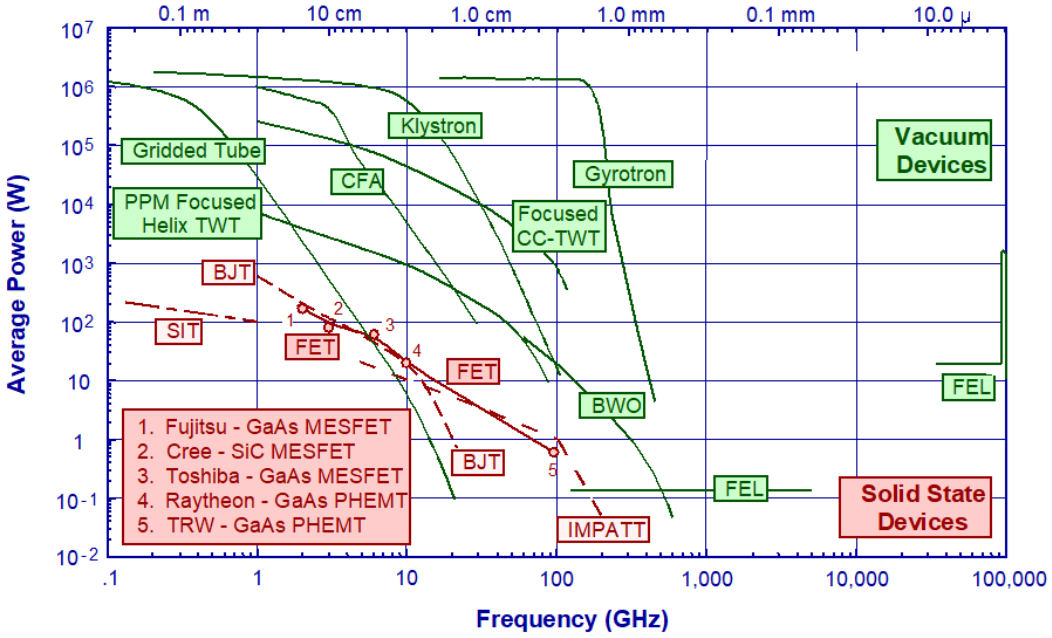


Figure 1.2: Frequency-power plot showing the technological range of different types of EM wave sources. The vacuum electronic devices shown include the gyrotron, klystron, travelling-wave tube (TWT), crossed-field amplifier (CFA), free-electron laser (FEL), and backwards-wave oscillator (BWO). Figure taken from [7].

limits the power-handling capabilities, and the system dimensions scale with the wavelength. High-frequency operation means a small wavelength, thus a small system design, leading to high system heating. High-power operation is thus severely limited at high frequencies. On the other hand, gyrotrons are always of much larger dimensions, and have less (not zero!) issues handling the high internal power density [13, p.589].

### 1.2.2 Operating principle

The operating principle of a gyrotron is as follows [5], refer to Figure 1.3 for a sketch of a gyrotron's cross-section. The magnetron injection gun (MIG) at the bottom of the gyrotron emits electrons into the vacuum of the gyrotron. The electrons are accelerated over a large voltage difference, and guided into a beam by a strong magnetic field, generated by a superconducting magnet that surrounds the bottom-half of the gyrotron. The beam excites a high-harmonic standing EM wave in the resonance cavity. The EM wave is guided by a wave launcher towards a mirror system. By the interaction the wave undergoes with the wave launcher, the wave becomes almost purely gaussian. The mirrors guide the wave to the output window. After the window, the wave enters a waveguide, and is directed to the fusion reactor. The electron beam loses approximately half of its energy in the resonance cavity, and continues to propagate upwards through the gyrotron. The beam is stopped in the collector.
The MIG emits the electrons from a ring-shaped emitter. The emitter is heated by an internal filament, which is a resistive material connected to a low-voltage power supply. The large voltage difference over which the electrons are accelerated occurs between the cathode (which is the MIG) and the anode. The electrons are guided into the beam before they reach the anode.

### 1.2.3 Electron emission

In general, electrons can escape from their metallic structure if their energy is sufficiently high enough to overcome the metal's work function. For the gyrotron emitter, this energy is provided by heating

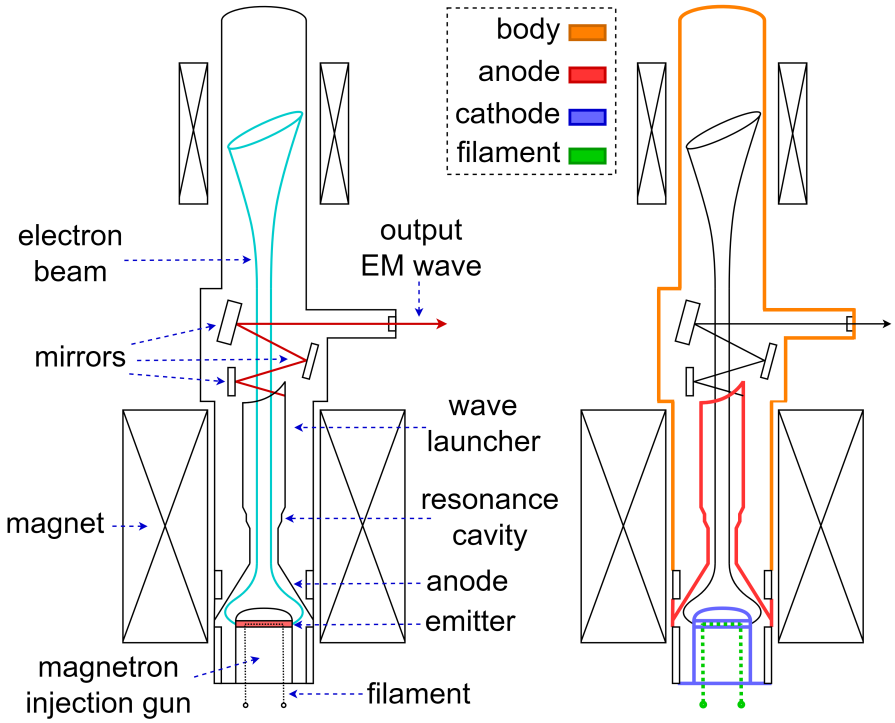


Figure 1.3: Schematic cross-section of an EU ITER gyrotron (not to scale). The gyrotron is approximately three meters high. The colours on the right indicate the voltage at which the components operate. Typically, the body voltage is at ground potential, the anode voltage is at +30kV, and the cathode voltage is at -50kV. The filament voltage is a low voltage, around 20V.

(thermionic emission) and the accelerating electric field (field emission) [13, ch.5]. Typically, the emitter is created from porous tungsten, which is impregnated with a low-work function metal or alloy, such as barium-oxide.
The current that arises from the emitter is thus a function of both the accelerating voltage, and the emitter temperature. Figure 1.4 shows some typical lines of emitted current density as a function of these two parameters. This behaviour is separated in three regimes [14] [13, ch.5].

In the space-charge-limited (SCL) regime, the current density is limited by the acceleration voltage. In this regime, the electric field is not strong enough to drive away all electrons that have been emitted. The lingering electrons form a space-charge cloud around the emitter, and shield newly-emitted electrons from being accelerated in the electric field.
If the acceleration voltage is increased, the emitter enters the temperature-limited (TL) regime, in which the electrons are also emitted by the thermionic effect. However, in this regime, the electric field is strong enough to drive away all emitted electrons, and the beam current almost saturates. The current is increased by applying more heating power to the emitter, thereby allowing more electrons to be emitted.
If the acceleration voltage is increased much further (note the break on the horizontal axis of Figure 1.4), the emitter enters the field-emission regime. In this regime, the energy of most electrons is high enough to escape the metal, and the current density increases unbounded. The emission that occurs here is thus not due to the thermionic effect, but due to field emission, which is a quantum-mechanical tunneling effect. This regime is usually reached when the electric field at the cathode is above $10^9 \mathrm{Vm}^{-1}$ [13, p.47].

Gyrotrons usually have an acceleration voltage of approximately 80kV, leading to an electric field at the cathode around $5{\cdot}10^6$ $\mathrm{Vm}^{-1}$ [14]. Gyrotrons operate in the temperature-limited regime [13, p.590]. In

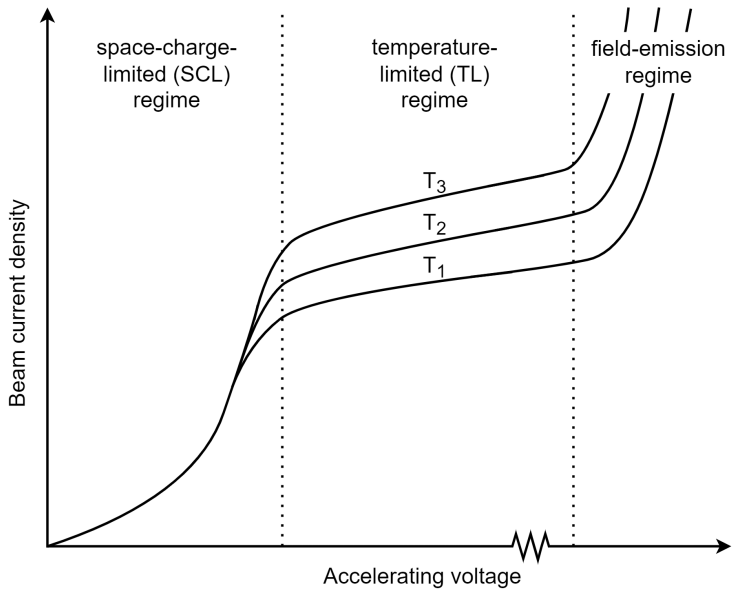


Figure 1.4: Sketch of the beam current density in the three emission regimes. In the TL regime, $T_3 > T_2 > T_1$. Figure adapted from [14] and [13, p.55].

this regime, the beam current $I_k$ is given by the Richardson-Dushman equation [14]:

$$I_k = 120 \cdot 10^4 A_{\mathrm{em}} T_{\mathrm{em}}^2 e^{-\frac{e(W_0 + cT_{\mathrm{em}} - \Delta W)}{k_{\mathrm{B}} T_{\mathrm{em}}}} \quad [\mathrm{A}], \tag{1.4}$$

where $A_{\mathrm{em}}$ [$\mathrm{m}^2$] is the emitter surface area, $T_{\mathrm{em}}$ [K] is the emitter temperature, $W_0$ [eV] is the material work function, $c$ $\left[\mathrm{eV} \cdot \mathrm{K}^{-1}\right]$ is a linear temperature correction coefficient, $\Delta W$ [eV] is a correction due to the Schottky barrier lowering, and $k_{\mathrm{B}}$ $\left[\mathrm{J} \cdot \mathrm{K}^{-1}\right]$ is the Boltzmann constant. Note how the beam current depends non-linearly on the emitter temperature. The value of the Schottky barrier lowering is given by [13, p.45]:

$$\Delta W = \sqrt{\frac{eE}{4\pi\epsilon_0}} \quad [\mathrm{eV}], \tag{1.5}$$

where $E$ $[\mathrm{V} \cdot \mathrm{m}^{-1}]$ is the electric field strength at the emitter surface, and $\epsilon_0$ $[\mathrm{F} \cdot \mathrm{m}^{-1}]$ is the permittivity of free-space. Note that the $-\Delta W$ term in Equation (1.4) is the reason that the beam current depends on the acceleration voltage in the temperature-limited regime.

### 1.2.4 Nottingham effect and associated problem

To summarise the discussion above: with a gyrotron, we have a power source that provides the fusion plasma with high-power high-frequency EM waves. By applying an accelerating voltage between the anode and cathode, and by heating the filament, the emitter will provide an electron beam current. The beam current is limited by the temperature of the emitter. The beam generates the requested EM wave in the resonance cavity and is thus important for the gyrotron operation.
The physics of the gyrotron as described here takes place on a time scale which is in the order of milliseconds or below. Up to recent years, the EU gyrotron research was focused on short pulses ($< 5$ms) to test gyrotron operation and optimise the design. Eventually, the gyrotrons in ITER will be operated continuously for long pulses ($> 1000$s). When extending the pulses to these timescales, new problems arise. One such problem is the focus of this research, and arises mainly due to the *Nottingham effect*.

When operating a gyrotron for long pulses at constant inputs to the MIG (acceleration voltage and

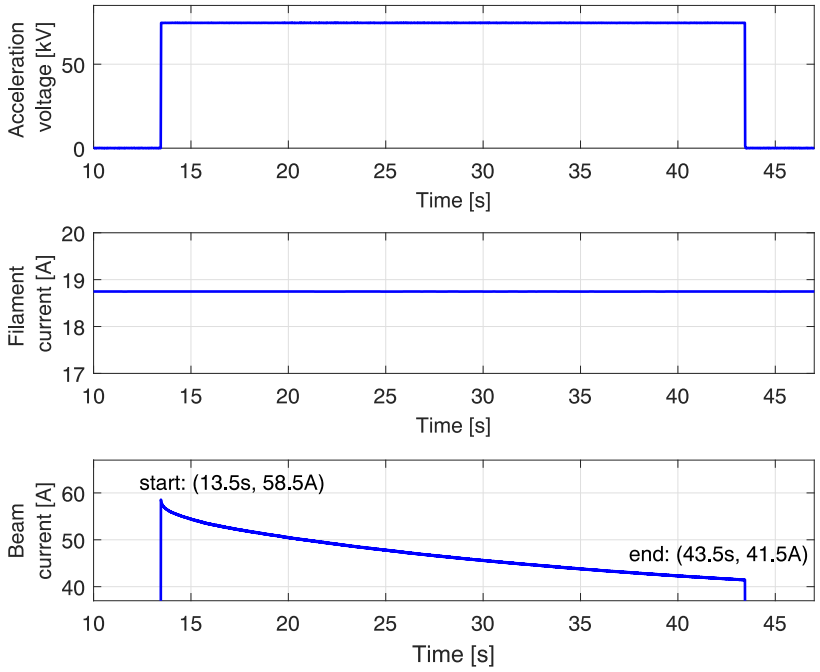


Figure 1.5: Experimental result of gyrotron TH1509U, Shot 10638, that showcases the Nottingham effect. For constant inputs to the MIG (acceleration voltage and heating power via the filament current), the beam current decreases by 29% in 30 seconds.

heating power to the filament), the value of the beam current does not remain constant. Over the course of tens of seconds, the current can reduce to 70-80% of its requested value. An example of this behaviour is shown in Figure 1.5 for an EU ITER gyrotron.
The physical reason for the decrease in current is as follows: in the SCL and TL regimes, the electrons are emitted by the thermionic effect. The electrons overcome the metal work function by the thermal energy provided by the emitter's heat. However, this work function is the *minimum* energy necessary to escape the metal. The electrons' thermal energy is increased *above* this minimum. Hence, the electrons take some excessive thermal energy with them when they escape the metal. The amount of heat that the electrons remove from the emitter is given by [14]:

$$Q_{\text{beam}} = I_k(2k_{\text{B}}T + W_0 + cT - \Delta W) \quad [\text{W}]. \tag{1.6}$$

This heat loss causes the emitter to cool down, if the filament heating power is kept constant. As the gyrotron is operated in the TL regime, cooling down the emitter leads to a lower emitter current. In turn, the lower beam current leads to less cooling-down. This limits the cooling of the emitter to a certain level. An equilibrium is thus reached between heating the filament, and the cooling of the emitter by the electrons. The heat loss due to the electron beam is called the Nottingham effect, named after W. Nottingham [15] [16].

The Nottingham effect thus causes the beam current to deviate from its set value. This leads to two major problems for the gyrotron operation:

1. a drop in beam current leads to a drop in the gyrotron's output power. This is of course unwanted, as more gyrotrons are needed for the same fusion operation. This leads to a strong increase in costs, as gyrotrons are costly devices (e.g. 1 million euro each), and it becomes more difficult to synchronise all gyrotrons to operate simultaneously.

2. due to the physics in the resonance cavity of the gyrotron, a change in beam current can lead to

a complete loss of output power. There is a large number of modes that can be excited in the resonance cavity. The beam current has a strong influence on which mode is excited. This poses problems, both directly and indirectly. In a direct way, if the beam current varies too much, the requested mode is not excited anymore, and the output power is completely lost. In an indirect way, if the beam current varies too much, unstable modes can be excited, which can damage the gyrotron and require a restart of the gyrotron [7].

These problems make that the EU ITER gyrotrons can be unreliable in the EC system at ITER. It is thus crucial that this issue is solved before ITER is commissioned.

## 1.3 Current state of research

### 1.3.1 Current solution to the problem

The current solution to the decreasing current, is to apply a so-called *boosting sequence*. In such a sequence, a series of incremental-steps is applied to the acceleration voltage and/or the filament current. A step applied to the acceleration voltage immediately leads to a small step in beam current, due to the Schottky barrier lowering. However, the voltage can not be varied too much, as this influences the mode excitation as well. A step applied to the filament current takes several tens of seconds to lead to an increase in beam current, but it is less restricted than the voltage step. An example of a boosting sequence and its effect on the beam current is illustrated in Figure 1.6.
Long pulses have been generated on gyrotron TH1509U using boosting sequences. Pulses of up to 1000s have been recorded. However, the sequences need to be pre-programmed. This poses issues when the shape (amplitude, duration) of the requested pulse is changed during operation, which it will as at ITER the gyrotrons need to be able to operate in an intermittent way for instability control. Furthermore, the gyrotron is sensitive to its initial conditions: a heating sequence might work for a specific pulse, but might not work for the same pulse shape at a different moment in time. Last, creating a boosting sequence requires a lot of experimental knowledge. Hence, using boosting sequences is an unsuitable solution to be used in ITER.

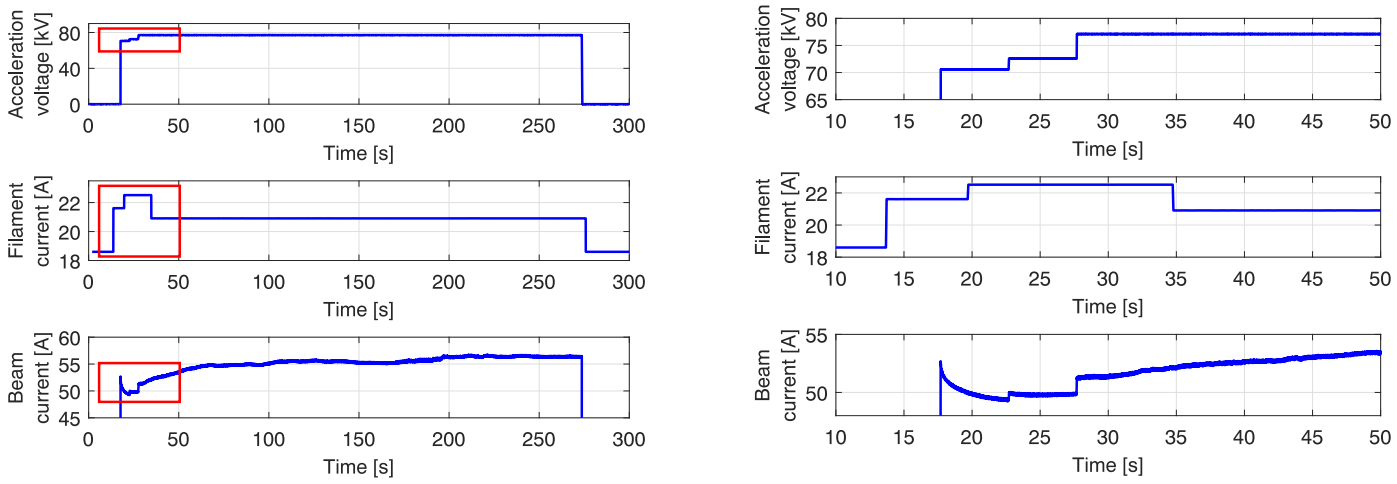


(a) complete pulse

(b) zoomed in at the start of the pulse

Figure 1.6: Experimental result of gyrotron TH1509U, Shot 10014, that shows how a boosting sequence is used to mitigate the Nottingham effect. In this example, steps are applied to both the acceleration voltage and the filament current in the boosting sequence. The steps in voltage are immediately visible in the beam current. The steps in the filament current take time to lead to an increase in beam current.

### 1.3.2 Proposed solution and previous work

A better solution to the problem would be to have a *real-time feedback-based* control system that automatically influences the two MIG-inputs (acceleration voltage and filament current) to maintain a stable beam current. The first step to developing such a control system is to construct a model of the MIG. Some work has already been done in this direction by a Ph.D. student and a master's student from the Polytechnic University of Milan. Nicolò Badodi initiated the work in 2021 by constructing a lumped-element model that represents the MIG's emitter [14]. Badodi justifies modelling the emitter as a lumped-element model by using FEM simulations to show that the temperature is approximately constant in the entire emitter. In 2022, Ruggero Bertazzoni continued the work by constructing a lumped-element model that includes more components of the MIG [17]. This last model is implemented in Simulink, a MATLAB subprogram.

## 1.4 Research setup

In this research, the work on this solution to the problem is continued. The goal of this research is to:

***design a simulated control system which utilises feedback to control the beam current of the EU ITER gyrotron.***

### 1.4.1 Methodology

First, the lumped-element model by Bertazzoni is discussed. Several changes are proposed to this *original* lumped-element model in an attempt to improve its performance and usability. The result of this is referred to as the *adapted* model. Second, an attempt is made to model the MIG in a different way, by considering it as a black-box system. Third, the MIG model is used to design a control system in Simulink, which is referred to as the *beam-current control system*. The beam-current control system is developed as far as possible, such that it could be implemented on the *general* control system of the EU ITER gyrotron. The general control system already exists.
The performance of the MIG models is determined based on the errors they produce when comparing their output to experimental data, referred to as *test data*. For each gyrotron shot, a value is given for the maximum error, the errors at the start and end of the pulse, and the RMS error, which is calculated as:

$$e_{\text{RMS}} = \sqrt{\frac{1}{N}\sum_{N}\left(I_{k,\text{exp}} - I_{k,\text{sim}}\right)^2} \quad [\text{A}], \tag{1.7}$$

with $I_{k,\text{exp}}$ [A] the experimental value of the beam current, and $I_{k,\text{sim}}$ [A] the simulated value of the beam current, which are evaluated at $N$ [-] time instants. A model will be considered to perform "good" when its $e_{\text{RMS}} < 0.5$A for various test shots. The test shots that are used in this study are listed in Appendix A.
For the control system, the closed-loop stability is measured based on the gain and phase margins. As the system is non-linear, use is made of the Matlab System-Linearizer tool for various operating points. For each linearisation, the gain margin (GM) and phase margin (PM) are then easily determined from a Nyquist plot, that is constructed using the open-loop transfer [18]. Based on general control engineering principles [19], the system is considered to be sufficiently stable if: GM $>$ 1.5dB and PM $>$ 20°.

### 1.4.2 Design requirements

As this research has a design goal, it is important to define several design requirements. The following *mandatory* design requirements are identified, which the design must satisfy:

M1 The control system has a stable closed-loop response.

M2 Only the filament current may be used as an actuator in the control system. The acceleration voltage is considered to be a given value.

M3 The control system keeps the beam current within ±10% of the reference value at all times, this is referred to as the *reference margin*.

M4 The control system controls the beam current with a steady-state error of less than ±1%.

M5 The control system varies the filament current with a maximum slope, which depends on if the filament is hot or cold: 0.1A/s (hot filament) or 0.01A/s (cold filament). The filament is considered hot if $I_f \geq 5$A, or cold if $I_f < 5$A.

M6 Besides the maximum slope, the control system may apply steps to the filament current if the filament is hot. These steps have a maximum amplitude of 5A and are separated by at least 10s.

M7 The control system provides the control as specified above for three operating scenarios: (1) a step-shaped reference in the range of 40-60A with a constant acceleration voltage in the range of 60-100kV, (2) small steps applied to the acceleration voltage during the step-shaped pulse (5kV steps, separated by at least 10s), and (3) a modulated acceleration voltage during the step-shaped pulse, with a modulation frequency of at most 1kHz.

Besides these requirements, also the following *design aspects* are identified, for which the design can be optimised:

D1 The beam current's settling time is as short as possible.

D2 The design of the control system is as general as possible. The control system should thus be utilisable with minimum effort on other gyrotrons than the EU ITER gyrotron.

### 1.4.3 FALCON test facility

The research is performed for the EU ITER gyrotron at the FALCON test facility. This test facility is located at the Swiss Plasma Centre (SPC) on the campus of the École Polytechnique Fédérale de Lausanne (EPFL), Switzerland. The FALCON test facility is used in the Fusion for Energy (F4E) gyrotron programme. The facility features an EU ITER gyrotron (TH1509U), and includes auxiliary systems, such as: a high-voltage power supply, an emitter-filament power supply, wave guides, optical systems, and dummy loads [20].
In this research, the beam-current control system will not be implemented and tested on the gyrotron's general control system. As mentioned before, the general control system for operating the gyrotron already exists, and is implemented at the test facility. The beam-current control system will be developed in this research such that it can be implemented as a short algorithm on the general control system.

### 1.4.4 Thesis outline

This thesis is structured as follows. In Chapter 2, the adapted lumped-element model is discussed. This contains all the changes made to the original model. The performance of the adapted and the original model is compared here too. In Chapter 3, the black-box modelling approach is considered. This model is also compared here with the lumped-element models. In Chapter 4, the beam-current control system is designed, and its results are shown. In Chapter 5 a conclusion on the performed work is given. Last, in Chapter 6 mentions numerous recommendations for further development of the MIG models and the beam-current control system. Appendix A lists the gyrotron shots that are used as test data in this research.

# Chapter 2: Lumped-element MIG models

As mentioned, part of the focus of this research is on several ideas to change the original lumped-element model, in order to increase its performance and usability. This is motivated by the original model's unsatisfactory performance, keeping in mind the condition for a "good" model as mentioned in Subsection 1.4.1: only 14 out of 95 high-power shots of Appendix A satisfy this condition. To illustrate, Figure 2.1 shows two examples of the beam current as predicted by the original model: one shot where the output is predicted well ($e_{\mathrm{RMS}} = 0.15$), and one shot where the output is predicted poorly ($e_{\mathrm{RMS}} = 1.95$A). Another motivation to make changes to the original model is that the model is unsuitable to be used in the simulated beam-current control system, as it uses the filament *power* as input, instead of the required filament *current*.
Before implementing the changes to the original model, the structure is discussed that the original and the adapted models have in common.

## 2.1 Common structure of the lumped-element models

Figure 2.2 shows a conceptual cross-section of the MIG. The MIG contains several components, suspended in vacuum:

- The filaments, which are surrounded by electrically-insulating alumina rings. The filaments carry an electric current, and heat up due to their resistance. This heat is transported to the other components by radiation.
- The emitter, which emits electrons into the gyrotron.
- Two sets of heat shields, referred to as the upper shields (left) and the lower shields (bottom). These aim to reflect as much heat as possible to the emitter, and minimise losses.

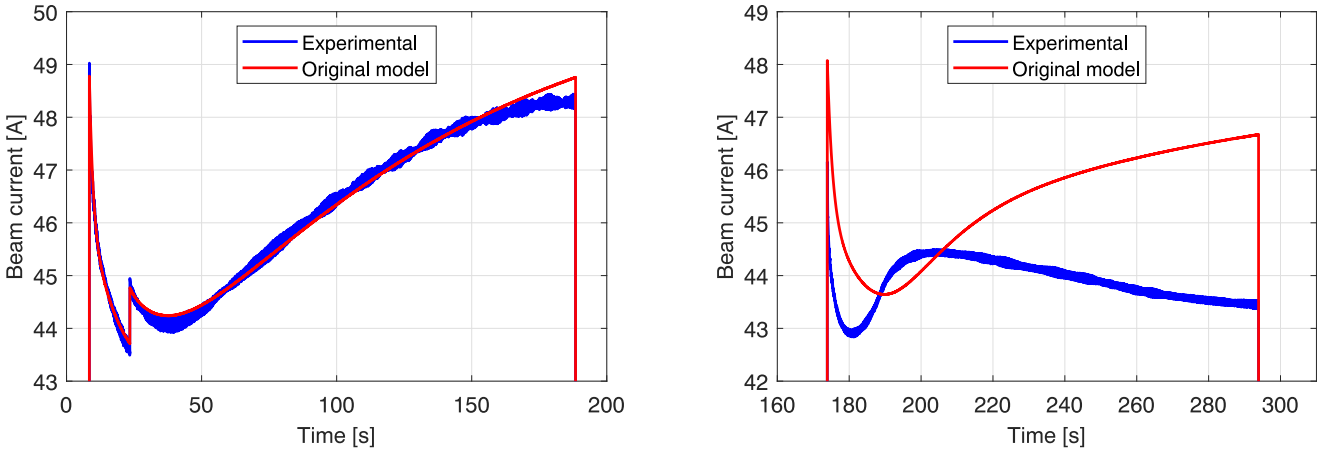


Figure 2.1: The output of the original lumped-element model for Shot 9680 (left, $e_{\mathrm{RMS}} = 0.15$A) and Shot 10802 (right, $e_{\mathrm{RMS}} = 1.95$A).

- A larger metallic structure containing the other components, which is arbitrarily separated into two parts: the nosecone (the top of the MIG) which shapes the electric field outside of the MIG; and the prolongator (the bottom of the MIG) which is connected to the rest of the gyrotron and provides mechanical support.

In the lumped-element models, the MIG components are considered to be lumped elements: each has a zero-dimensional mass and temperature. The models calculate the radiative heat flows between adjacent components based on the Stefan-Boltzmann law and pre-determined view factors. The heat flows are calculated in two artificial "heat exchangers". The components' temperatures are then updated as:

$$\Delta T = \frac{Q_{\text{net}}}{mc_h}\Delta t \quad [\text{K}], \tag{2.1}$$

with $\Delta T$ [K] the change in the component's temperature, $m$ [kg] the component's mass, $c_h$ [J/kgK] the specific heat of the component's material, and $\Delta t$ [s] the size of the simulation's time-step. $Q_{\text{net}}$ [W] is the net heat flow the component receives: the incident heat minus the heat the component radiates itself. It takes approximately 30-50s for a temperature change in the filaments to lead to a temperature change in the emitter, and it takes approximately 1000s before all components reach a steady-state temperature.
Different from the other components (which all have only one lumped temperature), the emitter is considered to consist of three parts, each with its own temperature: a large bulk part, and two artificial layers at the electron-emitting surface. These layers allow a faster transient of the emitter surface temperature at the pulse start, than when the emitter is considered as only one part. The heat flow between the three emitter parts is subjected to a thermal resistance.
The models have two inputs: the power supplied to the filaments, and the acceleration voltage. Both inputs are given by data from past experiments on gyrotron TH1509U. The models calculate the predicted beam current as output, which is then compared to the experimental beam current, as was done in Figure 2.1.
Besides using data from the MIG (view factors, masses), the models contain various *tuning parameters*. These parameters (should) represent some physical parameter of the MIG, which is too difficult to measure or model. At the end of constructing the model, the parameters are tuned to let the model have

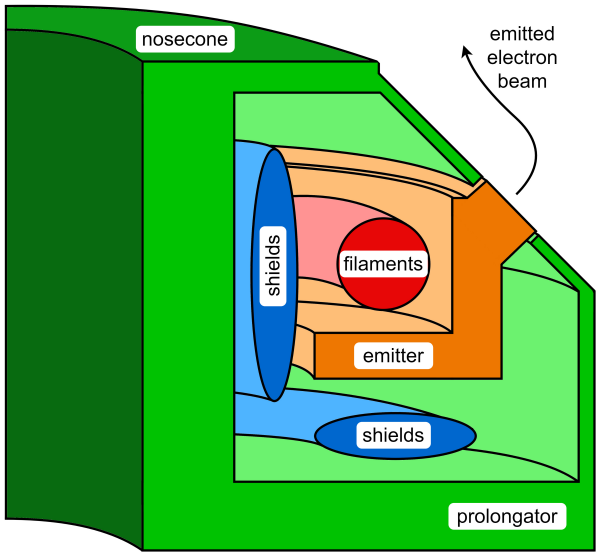


Figure 2.2: A conceptual cross-section of the right-half of the MIG. The electron beam is emitted outwards from the top-right edge of the emitter. The MIG is azimuthally symmetric around the left side of this image. This half cross-section is a few centimeters large in reality.

the best match with experimental data. The data that is used for this purpose, is referred to as *training data*. The tuning parameters are discussed further in Subsection 2.2.4.

## 2.2 The adapted model

An overview of the structure of the lumped-element models is shown in Figure 2.3. This overview shows several numbered items indicated in red: these are the changes I made. These changes are summarised below, with their numbers corresponding to the red numbers in the figure. In the adapted model:

1. the (number of) filaments and alumina are implemented according to the information provided by Thales. The code for this change is similar to other parts of the model, hence, this change is not discussed here further.
2. the prolongator and nosecone are modelled using a dynamic temperature, like the other components. This change is not discussed here further. The code for this change is similar to other parts of the model, hence, this change is not discussed here further.
3. the filaments can be modelled using their temperature-dependent resistance. This allows the model to consider the filament *current* as input, instead of the filament *power*. This change is necessary to use the model in the simulated control system later on in this research.
4. a new set of view factors is used, which satisfies conservation of energy.
5. the three components that are visible on the outside of the MIG (emitter, nosecone, and prolongator) experience a new heat loss, caused by the power these components radiate out of the MIG, towards other gyrotron components that surround the MIG (e.g. the anode).
6. a different set of tuning parameters is used. The parameters are tuned within bounds that ensure the parameters have a realistic physical interpretation.

All changes are significant to the model dynamics. Furthermore, changes 3-6 require an in-depth discussion, and are treated individually in the following subsections.

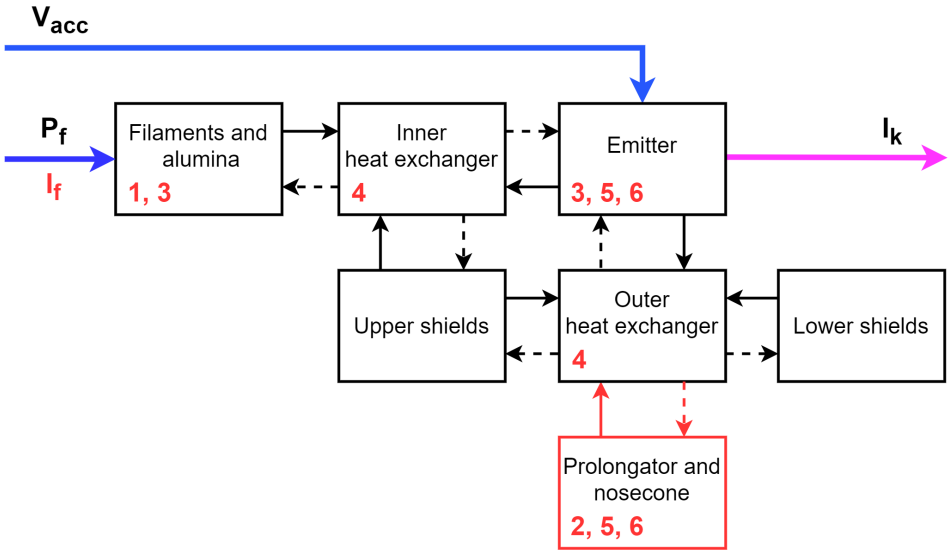


Figure 2.3: A schematic overview of the lumped-element models. The changes from the original to the adapted model are indicated in red (the numbers correspond with the text of Section 2.2). The solid arrows indicate the components' temperatures, which are provided to the heat exchangers. The dashed lines indicate the heat flows that the components experience. These flows can be negative, making the flow in the opposite direction than is indicated here.

### 2.2.1 Filament resistance

In the adapted model, the filament resistances $R_f$ are implemented. Using these, the model can also accept the filament current as input, instead of only the filament power. Then, the filament voltage is calculated using Ohm's Law, and the resulting filament power ($P_f = I_f V_f$) is used as before.
The filaments are simple pieces of metal, the resistance of which is generally temperature dependent [21, ch.3]. The temperatures of the filaments are not measurable, but these are calculated in the model itself. To give an idea: for a typical high-power pulse, the filament temperatures vary by more than 100K during the pulse (e.g. $T_f = 1800 - 1900$K). Furthermore, the filament temperatures are approximately 500K lower during low-power pulses (e.g. $T_f = 1300 - 1400$K). Hence, it is important to implement the resistances as a function of temperature, $R_f = R_f(T_f)$.
As it is impossible to get a measurement of the filament temperature, $R_f(T_f)$ is constructed from a data fit with the resistance (experimental value) and the temperature (given by the model itself). The data fit is constructed from 16 high-power shots, which leads to:

$$R_{f,i} = 0.6411 + 0.7644 \cdot 10^{-3}\, T_{f,i} \quad [\Omega]\,, \tag{2.2}$$

with $i$ the number of the filament, and the filament temperature in [K]. Equation (2.2) is validated by comparing the calculated filament voltage to the experimental voltage. For the 95 high-power shots considered in this research (Appendix A), the calculated voltage shows a RMS error with mean 115mV (≈0.5% of flat-top voltage) and a variance 2.5mV, which is considered to fit very well.

### 2.2.2 Heat exchangers and view factors

As mentioned before, the models' heat exchangers calculate the heat flows between the components based on view factors. In general, a view factor $F_{1,2}$ [-] is the fraction of radiative power that Component 1 radiates to Component 2. View factors must always satisfy two rules [22, ch.13]:

$$\sum_j F_{i,j} = 1, \qquad \text{summation rule,} \tag{2.3}$$

$$A_i F_{i,j} = A_j F_{j,i}, \qquad \text{reciprocity rule.} \tag{2.4}$$

The first rule states that all view factors of one component must sum to 1. The second rule states that if Component 1 radiates power to Component 2, then Component 1 also receives a proportional amount of power from Component 2. This proportionality depends on the areas $A$ of the components.
In the original model, the view factors of both the inner and the outer heat exchanger do not satisfy these rules. This leads to a violation of conservation of energy. Hence, the adapted model uses a different set of view factors.
In general, it is a considerable effort to exactly calculate view factors, taking into account the specific three-dimensional geometry of the system. Due to time constraints, I estimated the view factors by a detailed two-dimensional cross-section of the MIG. The new view factors:

- satisfy the summation rule.
- satisfy the reciprocity rule. This is achieved by first estimating a view factor $F_{i,j}$, and then calculating $F_{j,i}$ using Equation (2.4). The value of $F_{j,i}$ is not estimated separately.
- from and towards the filaments (i.e. $F_{\text{fil},j}$ and $F_{j,\text{fil}}$) are uniform. The multiple filaments may twist around each other when going around the MIG in the azimuthal direction. It is therefore impossible to exactly know if one filament is closer to -for example- the emitter than another filament. Due to this decision, the temperatures of the filaments are all equal (for equal initial conditions), and therefore their resistances are too.

### 2.2.3 Power loss by MIG-external radiation

The lumped-element models are based on radiative-power calculations. However, the original model neglected the radiation that comes from the outside surface of the MIG. Three components radiate this MIG-external radiation: the emitter, the nosecone, and the prolongator. In the adapted model, a power loss is included for these components that considers the MIG-external radiation.
The power loss is implemented using the Stefan-Boltzmann law. The components outside of the MIG (e.g. the gyrotron's anode) are not considered further via view factors, to simplify the problem. These components will however radiate power back to the MIG. The power lost by external radiation is then (assuming a gray surface) [22, ch.1]:

$$P_{\text{rad,ext}} = A\epsilon\sigma\left(T_i^4 - T_{\text{ext}}^4\right) \quad [\text{W}], \tag{2.5}$$

where $A$ [m$^2$] is the area of the MIG-element (nosecone, emitter surface, prolongator), $\epsilon$ [-] is the component's emissivity, $\sigma$ $\left[\text{Wm}^{-2}\text{K}^{-4}\right]$ is the Stefan-Boltzmann constant, $T_i$ [K] the component's temperature, and $T_{\text{ext}}$ [K] is the temperature of the components external of the MIG. The external temperature is assumed to be at room temperature ($T_{\text{ext}} = 293$K), as the anode -and other components- are cooled by oil circuits to this temperature. During a long high-power pulse, $T_{\text{ext}}$ could get up to 320K. However, this would hardly influence the value of $P_{\text{rad,ext}}$, as typical temperatures of the nosecone and prolongator are above 800K, and the emitter surface is around 1250K.

#### Reabsorption of MIG-external radiation due to reflections

It is important to note that the anode -and surroundings- are metallic. Hence, besides radiating power back to the MIG by its non-zero temperature $T_{\text{ext}}$, the anode also reflects a part back of the radiation it receives from the MIG. At the MIG, part of this back-reflected radiation is reabsorbed, and the rest is reflected once more to the anode, and so forth. In the end, a significant amount of the radiation is reabsorbed by the MIG.
Consider the most extreme case, where two infinite parallel plates, Plate 1 and Plate 2, face each other, see Figure 2.4. Plate 1 has reflectivity $r_1$ and absorptivity $a_1 = 1 - r_1$. Likewise, Plate 2 has reflectivity $r_2$ and absorptivity $a_2$. For this example, Plate 1 is assumed to radiate thermal power $P_{\text{rad,1}}$. Part of this power will be directly absorbed by Plate 2, and part of this power will be reflected by Plate 2. As the planes are infinitely wide, the reflected radiation is always incident upon Plate 1. Plate 1 will reabsorb part of its own radiation, and reflect part of this radiation back again. This continues indefinitely.
The first reflection allows Plate 1 to reabsorb a fraction of $a_1 r_2$ of its radiated power. Also part of the second reflection on Plate 2 gets absorbed, this is $a_1 r_2^2(1 - a_1) \triangleq a_1 r_2^2 r_1$. The third reflection is then $a_1 r_2^3 r_1^2$. Summing these and infinitely many more terms gives the power that is being reabsorbed into Plate 1 (written as a fraction of the power that Plate 1 initially radiates by the Stefan-Boltzmann law):

$$\begin{aligned}
\frac{P_{re-abs,1}}{P_{rad,ext,1}} &= a_1 r_2 + a_1 r_2^2 r_1 + a_1 r_2^3 r_1^2 + ... \\
&= a_1 r_2 (1 + r_2 r_1 + r_2^2 r_1^2 + ...) \\
&= a_1 r_2 \sum_{i=0}^{\infty} (r_2 r_1)^i \\
&= \frac{a_1 r_2}{1 - r_2 r_1}, \quad |r_2 r_1| < 1.
\end{aligned} \tag{2.6}$$

The constraint on $|r_2 r_1|$ given by the geometric series is always satisfied, as $|r_2|, |r_1| < 1$.
In the case of the MIG, Plate 1 will be either the emitter, nosecone, or prolongator, and Plate 2 represents the anode and surroundings.

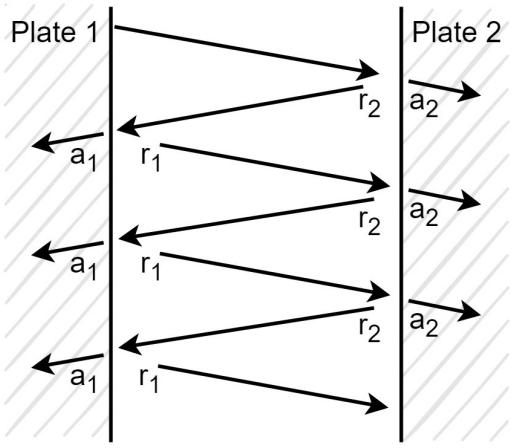


Figure 2.4: Two infinite parallel plates. Radiation is reflected between them, while parts get (re)absorbed.

The reflectivity and absorptivity of metals depend on the wavelength of the radiation [23]. The wavelength of the thermal radiation is assumed to be the peak wavelength $\lambda_p$ given by Wien's displacement law for a typical temperature $T_{\text{typ}}$ of the component. Table 2.1 summarises this information and the value given by Equation (2.6) for the anode, emitter, and nosecone/prolongator (equal for this purpose). Two values are reported for the anode, depending on if the anode is considered in front of the emitter (0.28), or the nosecone/prolongator (0.32). Clearly, the reabsorption effect has a significant impact on the net power that is radiated by these components. Note, the reported values are upper limits on the reabsorption-fraction, as Equation (2.6) assumes infinite parallel planes.

Table 2.1: Reabsorption of external radiation due to reflections, as given by Equation (2.6).

| Component | Anode | Emitter | Nosecone/prolongator |
|---|---|---|---|
| Material | Mb | W | Mb |
| $T$ [K] | 293 | 1250 | 800 |
| $\lambda_p$ [µm] | 9.89 | 2.33 | 3.62 |
| $r$ [-] | 0.944 | 0.874 | 0.895 |
| $a$ [-] | 0.056 | 0.126 | 0.105 |
| Reabsorption [-] | 0.28/0.32 | 0.68 | 0.64 |

### 2.2.4 Tuning parameters

As mentioned before, both lumped-element models contain tuning parameters. In the change from the original to the adapted model, some parameters are newly introduced, and all parameters are retuned. The goal of this is to obtain a better fit with the experimental data, and to use parameters that resemble a physical quantity, which was not considered in the original model. The tuning parameters of the adapted model are the following:

- A correction factor $f_{A,\text{em}}$ [-] is applied to the emitter's outside surface area. The correction factor accounts for the emitter's porous structure, which makes that the effective surface area is different than the measured surface area. The expected value of $f_{\text{A,em}}$ is in the range of 0.8-1.2.
- Three correction factors $f_{\text{reabs,em}}$, $f_{\text{reabs,nc}}$, and $f_{\text{reabs,pr}}$ [-] are applied to the MIG-external radiation losses of respectively the emitter, nosecone, and prolongator. These correction factors take into consideration that the reabsorption fraction of Equation (2.6) is derived for infinite parallel plates, while in reality a significant portion of the radiation is not reflected to the MIG. The possible values for $f_{\text{reabs,em}}$ are in the range of 1-3.125, and for $f_{\text{reabs,nc}}$ and $f_{\text{reabs,pr}}$ the possible values are in the range of 1-2.778, see the additional note below.

- Four parameters that concern artificial layers of the emitter. From the work of Bertazzoni, it already appeared that the emitter does not show a uniform temperature due to the fast heat loss by the Nottingham effect in the first few seconds of the pulse. Therefore, already in the original model, the emitter was implemented in three layers: a bulk layer, and two thin layers at the outside surface of the emitter. These layers are each characterised by a thermal capacitance $C_i$ (with $i = 1, 2$). Furthermore, there exists a thermal resistance $R_j$ between the three layers (with $j = 1, 2$). In the adapted model, these two $RC$-pairs are retuned, and bound by their physical interpretation as described below.

**Additional note regarding reabsorption correction factors**

The reabsorption is implemented in the model by considering a power loss in the emitter, nosecone, and prolongator as:

$$P_{\text{loss,net}} = \left(1 - \frac{a_1 r_2}{1 - r_1 r_2}\right) P_{\text{loss,SB}} \quad [\text{W}], \tag{2.7}$$

with $P_{\text{loss,SB}}$ the power loss that is given by the Stefan-Boltzmann law. This net power loss attains values in the range of:

- $P_{\text{loss,SB}}$ (no reabsorption) to $0.32 P_{\text{loss,SB}}$ (maximum reabsorption), for the emitter;
- $P_{\text{loss,SB}}$ (no reabsorption) to $0.36 P_{\text{loss,SB}}$ (maximum reabsorption), for the nosecone and prolongator.

In the adapted model, a correction factor is applied to Equation (2.7) to account for the fact that the MIG's and gyrotron's components are not infinite parallel plates. Three separate factors are used for the calculation of the net power loss of the emitter, the nosecone, and the prolongator. These correction factors have a range of:

- 1 (no reabsorption) to $\frac{1}{0.32} = 3.125$ (maximum reabsorption), for the emitter;
- 1 (no reabsorption) to $\frac{1}{0.36} = 2.778$ (maximum reabsorption), for the nosecone and prolongator.

As the correction factors are a geometrical factor, these are assumed to be equal for radiation going from the MIG to the anode, and vice versa. Hence, these factors are set also for the radiation from the anode to the MIG components due to the nonzero temperature of the anode (this radiation is used in the calculation of $P_{\text{loss,SB}}$). It would be more correct to consider separate factors for the anode-to-MIG radiation, but it would double the number of correction factors. As the power of the anode-to-MIG radiation is already much lower than the MIG-to-anode radiation (scales as $T^4$), there are only three independent correction factors: $f_{\text{reabs,em}}$, $f_{\text{reabs,nc}}$, and $f_{\text{reabs,pr}}$.

**Emitter layers**

The capacitances are related to the mass $m_i$ of the emitter layers. The resistances are related to the thickness $t_j$ of artificial "walls" between the layers that oppose the heat conduction. These values are calculated as [22, ch.3-5]:

$$m_i(C_i) = \frac{C_i}{c_{\text{em}}} \quad [\text{kg}], \tag{2.8}$$

$$t_j(R_j) = \frac{R_j A_j}{\rho_T} \quad [\text{m}], \tag{2.9}$$

with $c_{\text{em}}$ [J/kgK] the known heat capacity of the emitter's material, $A_j$ [m$^2$] the surface area of wall $j$, and $\rho_T$ [Km/W] the emitter's thermal resistivity. The wall area of the layers is assumed to be the outside surface area: $A_j = A_{\text{em}}$. For $\rho_T$, the value is taken from Powell *et al.* [24] for tungsten at 1250K: $\rho_T = 8.7 \cdot 10^{-3}$Km/W.

Table 2.2: The tuning parameters for the adapted lumped-element model as found by the optimisation algorithm. The values of $m_i$ are relative to the total emitter mass.

| Parameter | Value A | Interpretation A | Value B | Interpretation B |
|---|---|---|---|---|
| $f_{\mathrm{A,em}}$ [-] | 0.9 | em. area is decreased | 0.903 | em. area is decreased |
| $f_{\mathrm{reabs,em}}$ [-] | 1.05 | significant reabsorption | 1.058 | significant reabsorption |
| $f_{\mathrm{reabs,nc}}$ [-] | 1.05 | significant reabsorption | 1.06 | significant reabsorption |
| $f_{\mathrm{reabs,pr}}$ [-] | 1.05 | significant reabsorption | 1.059 | significant reabsorption |
| $R_1$ [K/W] | $1.9{\cdot}10^{-3}$ | $t_1 = 0.4$ [mm] | $28.0{\cdot}\ 10^{-3}$ | $t_1 = 5.8$ [mm] |
| $C_1$ [J/K] | 0.3 | $m_1 = 0.5$ [%] | 0.8 | $m_1 = 1.2$ [%] |
| $R_2$ [K/W] | $4.9{\cdot}10^{-3}$ | $t_2 = 1.0$ [mm] | $18.9{\cdot}10^{-3}$ | $t_2 = 3.9$ [mm] |
| $C_2$ [J/K] | 0.5 | $m_2 = 0.8$ [%] | 50.0 | $m_2 = 76.4$ [%] |

The values of $C_i$ that will be used in the model must result in $m_i$ that do not exceed the mass of the emitter itself. It is also important to subtract the masses $m_1$ and $m_2$ of the layers from the bulk mass $m_{\mathrm{em}}$. The values of $R_j$ that will be used in the model must result in $t_j$ that do not exceed the size of the emitter itself.
Layer 1 is considered to be on the outside surface of the emitter, and Layer 2 is considered to be in between the bulk layer and Layer 1. Layer 1 is assumed to be smaller than Layer 2, which leads to $C_1 < C_2$ and $R_1 < R_2$.

#### Tuning parameter optimisation

The adapted model is finalised by implementing all changes as discussed before in this section, and finding values for the tuning parameters. This is a non-convex optimisation problem in $\mathbb{R}^8$.
To solve this problem, a self-written optimisation algorithm is used, which is based on the steepest-decent method. An initial position $\mathbf{x_0}$ in the parameter space is chosen, with an associated function value $f(\mathbf{x_0})$. The optimisation is performed with three shots as training data (Shots 9722, 9948, 10826), and $f$ is set equal to the mean of the RMS errors $f = \mathrm{mean}(e_{\mathbf{RMS}})$. At each position, the gradient is approximated to the first order, and the new position in parameter space is calculated as [25]:

$$\mathbf{x_{new}} = \mathbf{x_{old}} - \alpha \nabla f(\mathbf{x_{old}}). \tag{2.10}$$

The step size $\alpha$ is determined using an Armijo condition.
The algorithm tries to find the global optimum by considering various initial positions. This becomes difficult, due to the long function-evaluation time (up to 1500s[1]) and large memory usage of Simulink. In the end, numerous local minima were found with parameter values within their bounds, but all with a non-satisfactory model performance. In Table 2.2 two sets of parameters are shown: Set A was initially found, and Set B was found from further optimising Set A. The model performs better with Set B (as discussed below), but the model is used with Set A later in this thesis (Chapter 4). Hence, both sets of parameters are listed here for completeness.
For both sets, all parameters are within their bounds, which allows a physical interpretation of them. However, the correction factors to the reabsorption are close to their lower bound, which indicates that the radiation losses are low (and thus a lot of reabsorption takes place). This is an unexpected result, but using larger values for these fractions leads to an almost-zero beam current.

## 2.3 Performance of the lumped-element models

To compare the performance of the original and the adapted lumped-element models (using Parameter Set B), the two most important errors are plotted for both models in Figure 2.5: the RMS error and

[1] On a regular laptop, with an Intel i7 core and 16GB RAM.

Table 2.3: Performance comparison of the original and adapted lumped-element models for the 95 high-power shots of Appendix A (both with Set A and Set B). Except for the RMS error, the relative errors are considered.

| | Original | | Adapted A | | Adapted B | |
|---|---|---|---|---|---|---|
| Error type | mean | var | mean | var | mean | var |
| RMS [A] | 1.84 | 1.59 | 2.07 | 1.04 | 1.61 | 1.19 |
| Relative max. [%] | 6.61 | 0.14 | 10.4 | 0.19 | 6.58 | 0.08 |
| Relative start [%] | 4.35 | 0.13 | 9.29 | 0.22 | 4.43 | 0.11 |
| Relative end [%] | 3.52 | 0.11 | 2.17 | 0.03 | 3.70 | 0.06 |

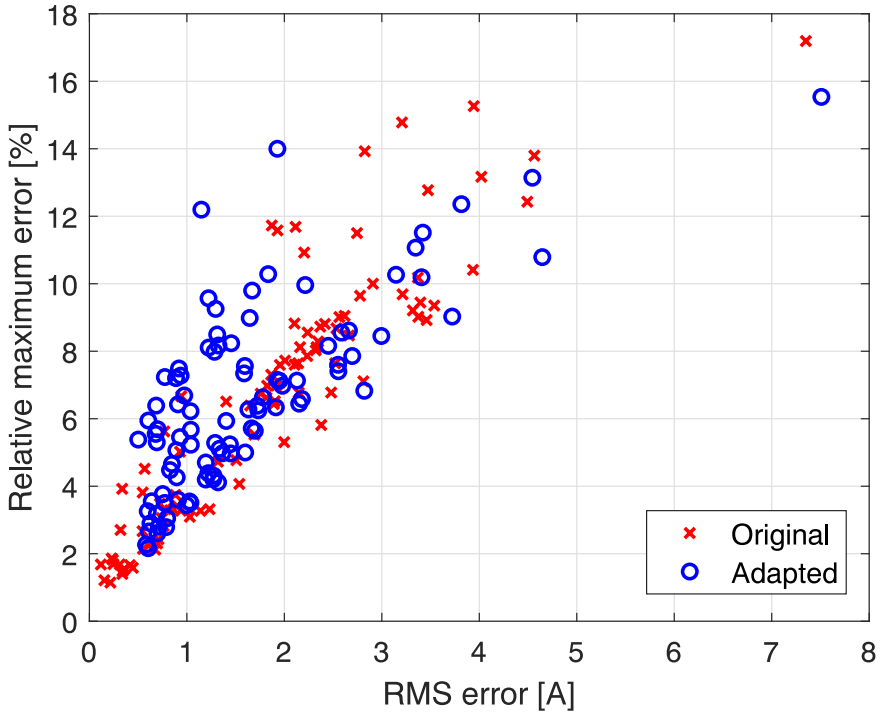


Figure 2.5: The RMS errors and relative maximum errors of the original and the adapted lumped-element model (using Set B) for the 95 high-power shots of Appendix A.

the relative maximum (absolute) error. These errors are also summarised for both models in Table 2.3 (using both parameter sets), including the relative error at the pulse start and pulse end. The adapted model (Set B) produces a smaller RMS error than the original model does, and comparable other errors (maximum, at pulse start, and at pulse end). Furthermore, the adapted model shows a significantly lower variance in the RMS errors than the original model does. As mentioned, both models do not give satisfactory results. Considering the definition of a "good" model of Subsection 1.4.1 (RMS error <0.5A), the original model shows a good result for 14 shots, the adapted model for none.

It is possible to further improve the adapted lumped-element model in various ways. This is discussed in the recommendations for further research in Chapter 5. In the next chapter, a different modelling approach is researched, which considers the MIG as a black-box model.

# Chapter 3: Black-box MIG model

In the black-box model, (almost) no assumptions are made on the physical processes inside the MIG, and a mathematical model is constructed based on input-output data. The black-box model is also a two-input one-output model, like the lumped-element models. Setting up a black-box model for the MIG is challenging due to:

- Challenge 1: the MIG is a non-linear system.
- Challenge 2: the future output values depend on the previous output values (Nottingham effect).
- Challenge 3: the system contains long delays. It takes a long time before a change in filament current is visible in the output, or for the Nottingham effect to occur.
- Challenge 4: the output is zero if either input is zero. It is thus impossible to set up experiments that display the effects of the inputs separately.

The MIG is modelled as a non-linear state-space model. The reasons for choosing this class of model above others are in short: transfer functions do not model the effect an output has on itself (Challenge 2), numerical time-domain methods would need to consider too many data samples at a time due to the long delays (Challenge 3), and analytic time-domain models would need to be designed for different sets of pre-defined steps in the inputs (becomes difficult to work with in a control system).
Besides this, in a state-space model, the states of the MIG could intuitively consist of the temperatures of the MIG components, and the Richardson-Dushman equation can be used to compute the beam current. For simplicity and by lack of measurements of internal temperatures, only the emitter temperature is used as state variable, and Equation (1.4) is used to calculate the model's output[1].

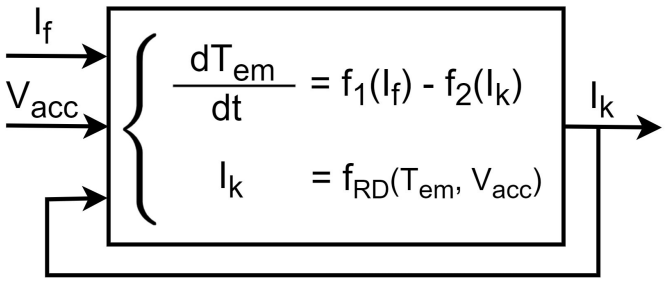


Figure 3.1: Schematic representation of the black-box model. The model uses the emitter temperature as its internal state, which is influenced by the filament current (input 1) and the beam current (output). The beam current is calculated from the emitter temperature (state) and the accelerating voltage (input 2).

[1] On the nomenclature: by using the Richardson-Dushman equation to calculate the beam current, the black-box model is technically a *gray*-box model. However, as the lumped-element models are also gray-box models, the state-space model is referred to as a black-box model to avoid confusion.

## 3.1 State-space design

The state-space model is shown schematically in Figure 3.1. At each time step, the model's state, the emitter temperature $T_{\text{em}}$, is updated using its time derivative. This derivative depends on two functions: the heating function $f_1(I_f)$ and cooling function $f_2(I_k)$, which are designed as follows. In this discussion, use is made of an "indirect measurement" of the emitter temperature: as from experiments the acceleration voltage and the beam current are known, it is possible to calculate which emitter temperature was necessary to produce the given beam current. For this purpose, Equation (1.4) is solved for $T_{\text{em}}$ iteratively.

### 3.1.1 The heating function

The heating function $f_1(I_f)$ must have a positive effect on the emitter temperature: a higher filament current leads to a higher emitter temperature. The rate of heating is proportional to the difference between the emitter temperature and the temperature that can be reached using a certain filament current, which is referred to as the target temperature: $f_1 \propto T_{\text{target}} - T_{\text{em}}$.
The target temperature is a function of filament current, $T_{\text{target}} = T_{\text{target}}(I_f)$. This function is found from a datafit, constructed from the experimental values of the emitter temperature and the preheating filament current (i.e. only one $T_{\text{em}}$ and one $I_f$ value per experiment). This method ensures that the temperature is considered before the Nottingham effect influences the emitter. The preheating filament current is the current that is applied for a long time before the pulse. This does not take into account any boosting sequences that have been applied. The method thus assumes that the filament current has been applied for a long time, and that the system has reached a steady-state. The values of $T_{\text{em}}$ and $I_f$ values are extracted from the 95 high-power shots and the 44 low-power shots of Appendix A. The result is a linear function, see Figure 3.2:

$$T_{\text{target}}(I_f) = 42.2 I_f + 471.5, \quad [\text{K}]. \tag{3.1}$$

The datafit shows a mean absolute error of 3.8K with a variance of 8.8K.
The dependence of $f_1$ on $(T_{\text{target}} - T_{\text{em}})$ is difficult to determine. It is not possible to try a separate data

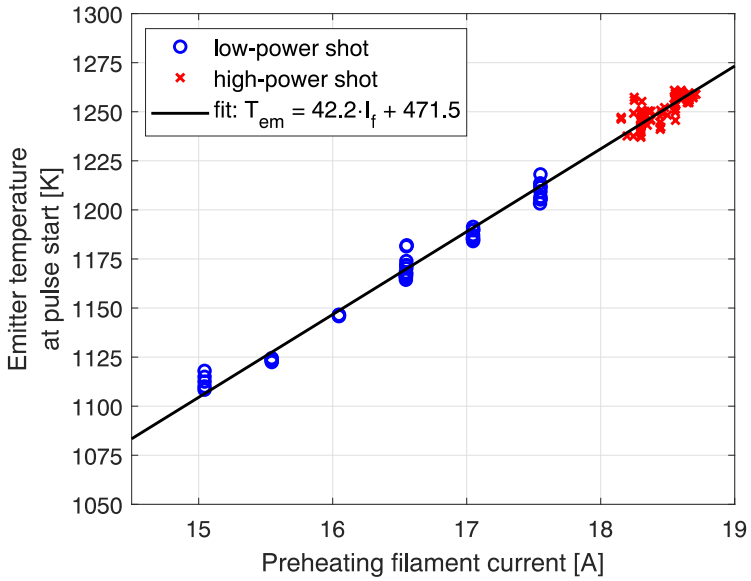


Figure 3.2: The emitter temperature at the pulse start as a function of the preheating filament current. Both variables are experimental values, due to the indirect measurement of the temperature.

fit for this relation, as the effect of $f_2$ is always present. In an initial attempt, the relation is assumed to be linear, with $f_1 = 0$ if $T_{\text{em}} = T_{\text{target}}$:

$$f_1(I_f) = c_1(T_{\text{target}}(I_f) - T_{\text{em}}), \quad [\text{K/s}]. \tag{3.2}$$

### 3.1.2 The cooling function

Next, the cooling function $f_2(I_k)$ must have a negative effect on the emitter temperature: a higher beam current leads to a lower emitter temperature. Note that the minus sign is included in the state equation (Figure 3.1), meaning that $f_2 > 0$. Again, it is difficult to find the dependence of $f_2$ on $I_k$, as the effect of $f_1$ is always present. Initially, the relation is assumed to be linear, and include the state $T_{\text{em}}$ itself:

$$f_2(I_k, T_{\text{em}}) = c_2 I_k T_{\text{em}}, \tag{3.3}$$

which closely resembles Equation (1.6). It is important that $f_2 = 0$ if $I_k = 0$, which is the case for this linear equation.

As the effect of the two equations can not be separated, the state-space model is optimised directly, using again a steepest-decent algorithm to find values for $c_1$ and $c_2$. The clear advantage over the lumped-element model becomes apparent here: the function evaluation time is less than one second. In the end, by using Shots 11074 and 11090 as training data, the following parameter values are found:

$$c_1 = 5.48 \cdot 10^{-3} \quad [1/\text{s}], \quad c_2 = 1.28 \cdot 10^{-5} \quad [1/\text{As}].$$

## 3.2 Results of the state-space model

The state-space model is tested on the 17 long low-power shots and on the 95 high-power shots of Appendix A. The results are summarised in Table 3.1. The performance of the original model is included for comparison. Clearly, the state-space model performs poor on the high-power shots, where the original model performs better. However, the state-space model performs much better on the low-power shots, where the original model is completely off.
This is a promising result, as the state-space model takes considerably less time and effort to design than the lumped-element model. However, it will be difficult to improve the performance of the state-space model beyond this point for the low-power pulses. Furthermore, no good result is found when trying to optimise the state-space model for high-power pulses. A different set of equations for $f_1$ and $f_2$ need to be found in order to find an appropriate state-space model for the high-power pulses. Hence, the black-box model as discussed in this chapter is unsuitable to be used in the development of the beam-current control system.

Table 3.1: Performance comparison of the original model and the state-space model for the long low-power and the high-power shots of Appendix A.

| | Original model | | | | State-space model | | | |
|---|---|---|---|---|---|---|---|---|
| | Low-power | | High-power | | Low-power | | High-power | |
| Error type | mean | var | mean | var | mean | var | mean | var |
| RMS [A] | 7.27 | 0.26 | 1.84 | 1.59 | 0.82 | 0.19 | 5.45 | 2.37 |
| Rel. max. [%] | 91.19 | 19.27 | 6.61 | 0.14 | 11.77 | 0.25 | 18.27 | 0.1 |
| Rel. start [%] | 66.47 | 7.82 | 4.35 | 0.13 | 6.26 | 0.31 | 8.02 | 0.28 |
| Rel. end [%] | 26.25 | 67.62 | 3.52 | 0.11 | 5.09 | 0.16 | 16.67 | 0.12 |

# Chapter 4: Beam-current control system

In this chapter, the beam-current control system is designed based on the adapted lumped-element model, with Set A of the tuning parameter values of Table 2.2 (as Set B was only found at a later time). The beam-current control system is implemented in Simulink. A sketch of the control loop is shown in Figure 4.1: it shows the simple feedback of the beam current to the reference signal, with an error signal as result. The error signal is the input of a controller, from where the next value of the filament current is determined. Three additional blocks are included that are important for the functionality of the beam-current control system:

- The **actuator limiter** ensures that the control system complies with Design Requirements M5 and M6: the filament current is limited in its slope, step size, and step timing.
- The **feedforward** provides an increase in filament current at the pulse start. This ensures that the control system complies with Design Requirement M3: the beam current must stay within ±10% of the reference.
- The **controller regulator** provides a smooth transition between the feedforward and the control signal, and thus also prevents a violation of Design Requirement M3.

The following two sections discuss the controller and the feedforward in-depth. Then, with a completed design, the control system is tested in the three operating scenarios of Design Requirement M7. The error introduced by the imperfect MIG model is discussed at the end of this section.
To explicitly clarify: measurement noise and actuator disturbances do not need to be considered in the control system, because the signal-to-noise ratio is very high for the acceleration voltage (≈33dB), the filament current (≈40dB), and the beam current (≈25dB), as can be seen from the pulse example of Figure 1.5. Furthermore, there are no significant delays expected on the actuator or the measurements.

## 4.1 Controller design

For the controller itself, a PID controller is considered. These types of controllers are used in many engineering applications, due to their simplicity in design, analysis, and implementation [26] [27]. The

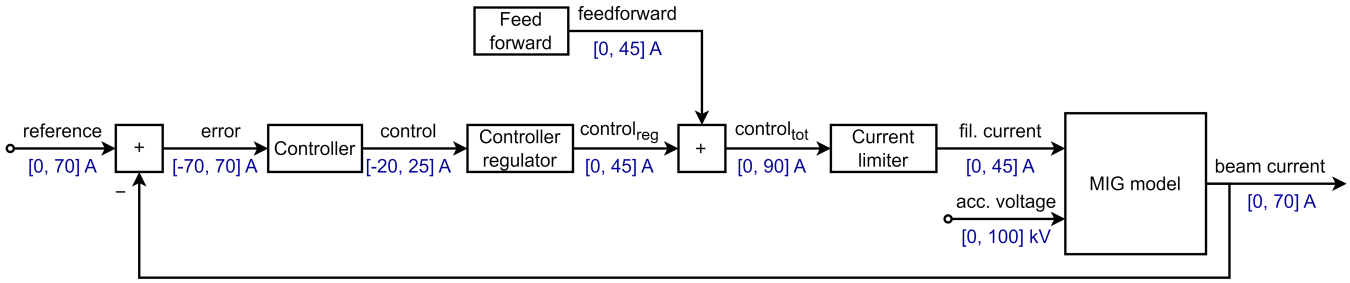


Figure 4.1: Sketch of the beam-current control system as it is implemented in the Simulink simulations. The ranges of the signal values are indicated in blue.

control signal $u(t)$ of a PID controller is given as:

$$u(t) = k_p e(t) + k_i \int_0^t e(\tau)\mathrm{d}\tau + k_d \frac{\mathrm{d}e(t)}{\mathrm{d}t}, \tag{4.1}$$

with $e(t)$ the error signal, and $k_p$, $k_i$, and $k_d$ the controller parameters. The controller is tuned manually, as online tuning is not possible at the gyrotron, and manual tuning is an intuitive method for this control loop. The tuning is performed in the following way:

1. At first, $k_p = k_i = k_d = 0$. The value of $k_p$ is slowly increased until the beam current starts to show damped oscillations.
2. With the value of $k_p$ fixed, $k_i$ is also slowly increased, until the steady-state error goes to zero sufficiently fast (e.g. within a few hundred seconds, the settling time is a non-mandatory design aspect).
3. In general, $k_d$ can then be increased to reach the steady-state value faster and smoothen the oscillations in the beam current. However, in this research $k_d = 0$, as the derivative term of Equation (4.1) causes problems when a voltage step is applied during the pulse, which is one of the possible operating scenarios (Design Requirement M7). The voltage step leads to a sudden step in beam current due to the Schottky barrier lowering (Equation (1.5)), causing a large spike in the time derivative of the error signal. From here on, the PID controller is referred to as a PI controller.
4. When the rest of the control system's design is finished, the PI parameters are adjusted to improve the stability properties of the system, if necessary.

For the final design, the following parameter values are used:

$$k_p = 0.8 \ \ [\text{-}], \quad k_i = 0.016 \quad \left[\mathrm{s}^{-1}\right], \quad k_d = 0 \ \ [\mathrm{s}].$$

## 4.2 Feedforward design

The feedforward signal is designed as the boosting sequences were designed for the high-power shots of Appendix A: the filament current is set to a preheating value long before the pulse starts. Around the pulse start, two steps are applied to the filament current. The steps add a few ampère to the preheating current for a few seconds. Different from the boosting sequences, the feedforward signal decreases from the second step's value to zero within two seconds. In the same time, the control signal is allowed to be increased by the controller regulator. See Figure 4.2.
The required preheating current is calculated from the required emitter temperature, similar to Equation (3.1). However, the linear relation is slightly different here, as a datafit is used to the model's emitter temperature, as opposed to the experimental emitter temperature. The feedforward step sizes and durations, and their timing with respect to the pulse start, are the design parameters of the feedforward. The final design is found by trial-and-error, and by evaluating the performance of the control system. It is found that the feedforward needs to be adjusted by a value $I_{\mathrm{adj}}$, based on the reference value to prevent a violation of Design Requirement M3. The final design uses:

$$\begin{aligned} &I_{\mathrm{pre}} = \frac{T_{\mathrm{em,req}} - 502.3}{41.3} \quad [\mathrm{A}], \quad I_{\mathrm{FF1}} = 20.5 + I_{\mathrm{adj}} \quad [\mathrm{A}], \quad I_{\mathrm{FF2}} = 24.5 + I_{\mathrm{adj}} \quad [\mathrm{A}], \\ &I_{\mathrm{adj}} = 0.06(I_{\mathrm{ref}} - 53) \quad [\mathrm{A}], \quad t_{\mathrm{FF1}} = 10 \quad [\mathrm{s}], \quad t_{\mathrm{FF2}} = 7 \quad [\mathrm{s}]. \end{aligned} \tag{4.2}$$

The effect and necessity of this feedforward becomes apparent from Figure 4.3, where the beam current is compared when no feedforward is used and when it is used.
This concludes the design of the control system. In the next three sections, the system is tested in the operating scenarios of Design Requirement M7.

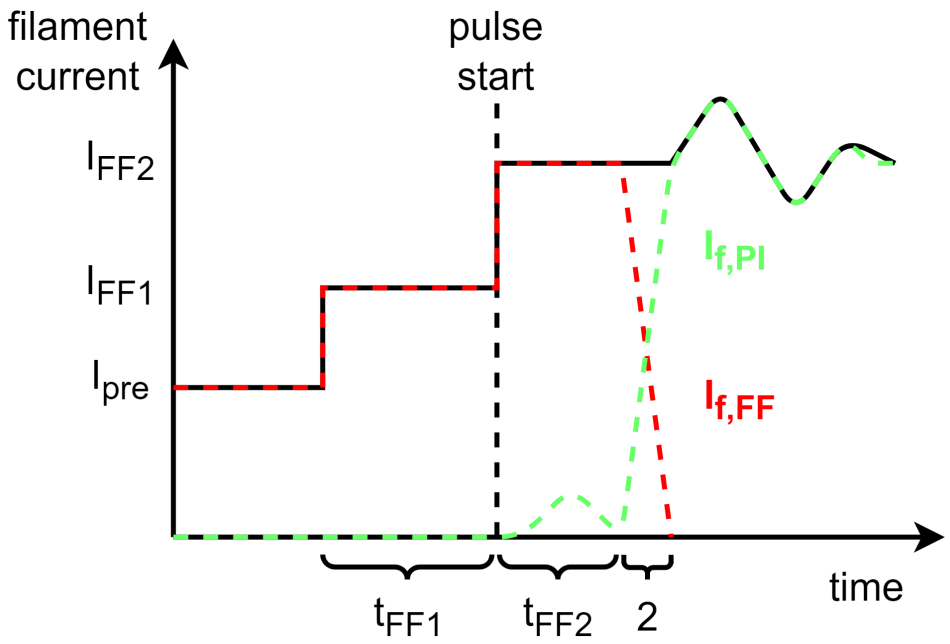


Figure 4.2: Feedforward signal $I_{f,\mathrm{FF}}$ and PI control signal $I_{f,\mathrm{PI}}$ around the pulse start. For a long time, the filament current is set to the preheating value $I_{\mathrm{pre}}$. The feedforward applies two steps to the filament current, at levels $I_{\mathrm{FF1}}$ and $I_{\mathrm{FF2}}$ for a duration of $t_{\mathrm{FF1}}$ and $t_{\mathrm{FF2}}$, respectively. In the final design, the feedforward is timed such that the second step occurs at the pulse start. After the second step, the feedforward decreases linearly to zero within two seconds. In this time, the controller regulator allows the control signal to be increased linearly too.

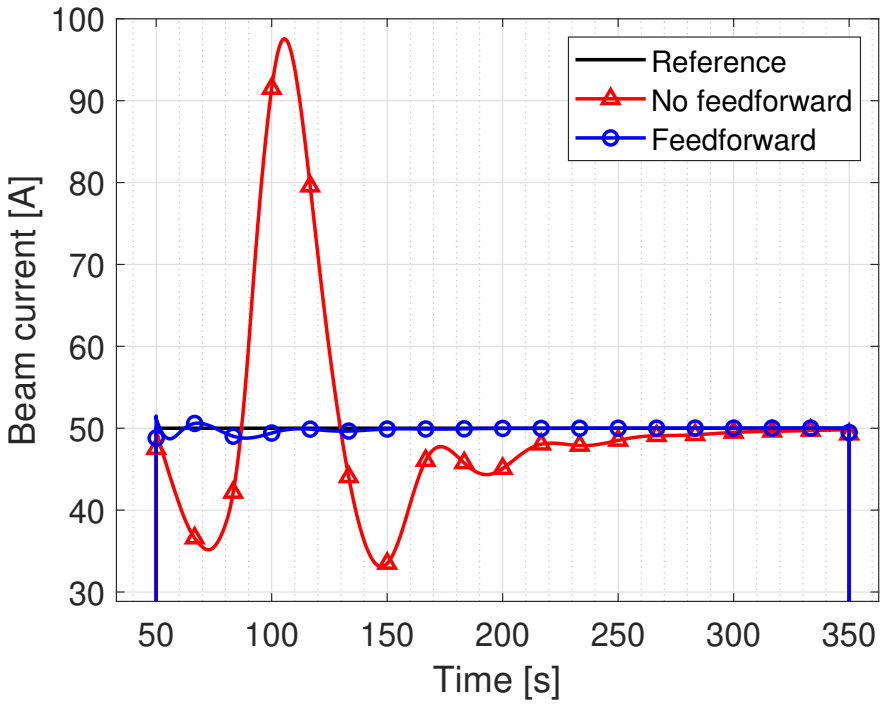


Figure 4.3: Control system output with and without feedforward. The feedforward prevents the beam current from dropping too low at the pulse start, and consequently prevents the controller from generating a too-large control signal which would cause the beam current to severely exceed the reference.

## 4.3 Control system performance: Operating Scenario 1

Using the design described above, the control system's performance is tested at various operating points in the operating space that is defined by Design Requirement M7: the system needs to be operational for reference values in the range of 40-60A, and acceleration voltages in the range of 60-100kV. The operation is checked at the edges and the middle of this operating space, giving nine operating points. The performance at these points gives a good indication of the performance in the whole operating region, as the beam current depends monotonically on the filament current and the acceleration voltage. For each operating point, it is checked that the beam current stays within ±10% of the reference (Design Requirement M3) and shows a steady-state error of at most ±1% (Design Requirement M4).
Figure 4.4 shows the beam current of the control system at the nine operating points. At all points, the beam current stays within ±4.1% of the reference and it shows no steady-state error (which is better visible for longer pulses).
To ensure that the control system is closed-loop stable, the gain margin (GM) and phase margin (PM) are computed at the nine operating points, in the way as described in Subsection 1.4.1. For an example of a Nyquist plot that is constructed for this purpose, see the additional note below.
The nine operating points show approximately similar margins. The minimum margins are observed for the operating point (60A, 100kV), and are:

$$\text{GM} = 11.4\ [\text{dB}], \quad \text{PM} = 27.1\ [^\circ].$$

These margins satisfy the imposed sufficient condition on stability. The control system is thus closed-loop stable around the nine operating points. As no unstable behaviour appears from simulations, and the beam current increases monotonically with filament current and acceleration voltage, the stability is assumed to hold in the whole operating space. With this result, the control system satisfies all mandatory design requirements for this operating scenario.

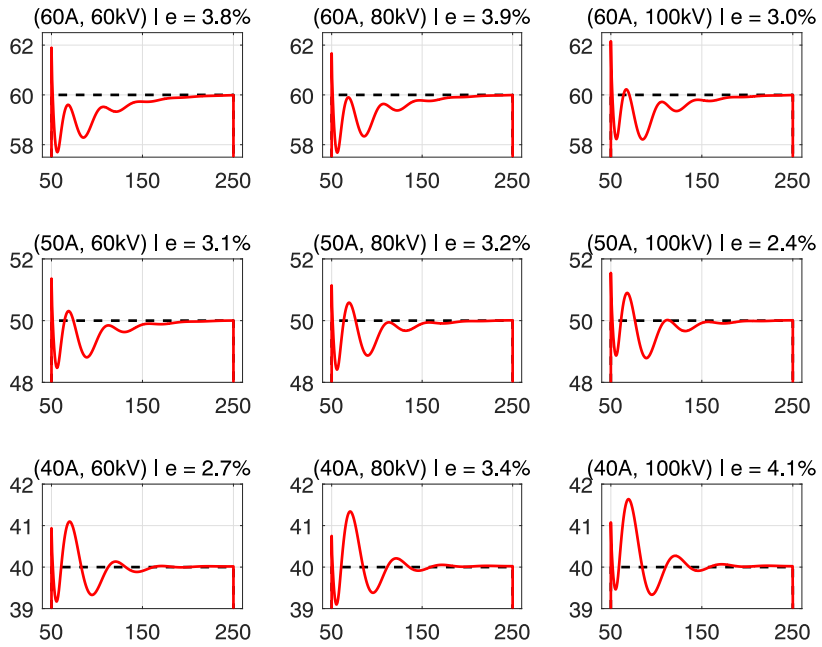


Figure 4.4: The beam current as produced by the control system at the nine operating points. All x-axes show the time [s], all y-axes show the beam current [A]. The reference is indicated with dashed black lines. The operating point is indicated above each plot in the format: (reference, acceleration voltage), where the rows show a constant reference, and the columns show a constant voltage. The maximum relative error is also indicated [%].

### 4.3.1 Nyquist plot example for stability margins

Figure 4.5 shows an example of a Nyquist plot. This plot was constructed from the open-loop transfer of the control system at a reference of 50A and an acceleration voltage of 80kV: the middle image of Figure 4.4.
At all operating points, the open-loop transfer is determined from the reference signal to the beam current, by applying small perturbations to the reference at eleven "snapshots" of the system. Each snapshot contains the values of all signals in the system at a given time instant during the simulated pulse: before the pulse, at the pulse start, during the pulse, at the pulse end, and after the pulse is over. The result is thus eleven separate systems and Nyquist plots. However, the systems show very similar behaviour, and only one is shown here for clearness.
The Nyquist plots must not encircle the $z = -1 + 0i$ point in the complex plane [18], as the open-loop transfer is considered, which has no poles in the right-half plane (the MIG itself is a stable plant). For each of the eleven systems, the minimum margins are considered. This is done for the nine operating points. Then, as a worst-case approximation, the minimum gain margin and the minimum phase margin are taken over all these 99 ($= 9 \cdot 11$) margins. These were the two values reported above (8.7dB and 24.6°). The example in Figure 4.5 has a gain margin of 12.6dB and a phase margin of 30.2°.
For clarity: these margins only indicate stability around the nine operating points. The stability is assumed to be valid for the entire operating space, as no unstable behaviour was seen in the simulations, the beam current depends monotonically on the filament current and the acceleration voltage, and the MIG itself is a stable system.

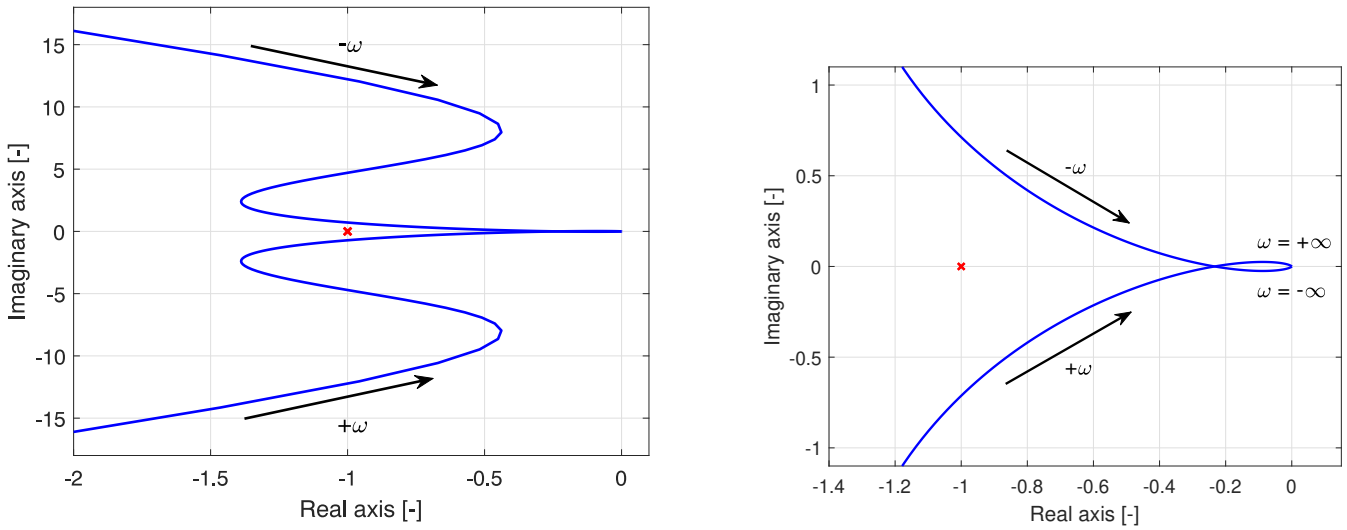


(a) zoomed out

(b) zoomed in

Figure 4.5: Nyquist plot as produced by the Matlab Model-Linearizer tool for a simulation of the control system at a 50A reference and a 80kV acceleration voltage. The red cross indicates the $z = -1+0i$ point. The incremental direction of the frequency is indicated (for both positive and negative frequency). This example shows only one linearisation around this point for clarity, instead of the eleven separate linearisations that are actually considered.

## 4.4 Control system performance: Operating Scenario 2

Besides a constant acceleration voltage, the control system also needs to be able to satisfy all mandatory design requirements for Operating Scenario 2: a varying acceleration voltage during the pulse. In this scenario, the voltage is varied in steps of at most 5kV, separated by at least 10s.

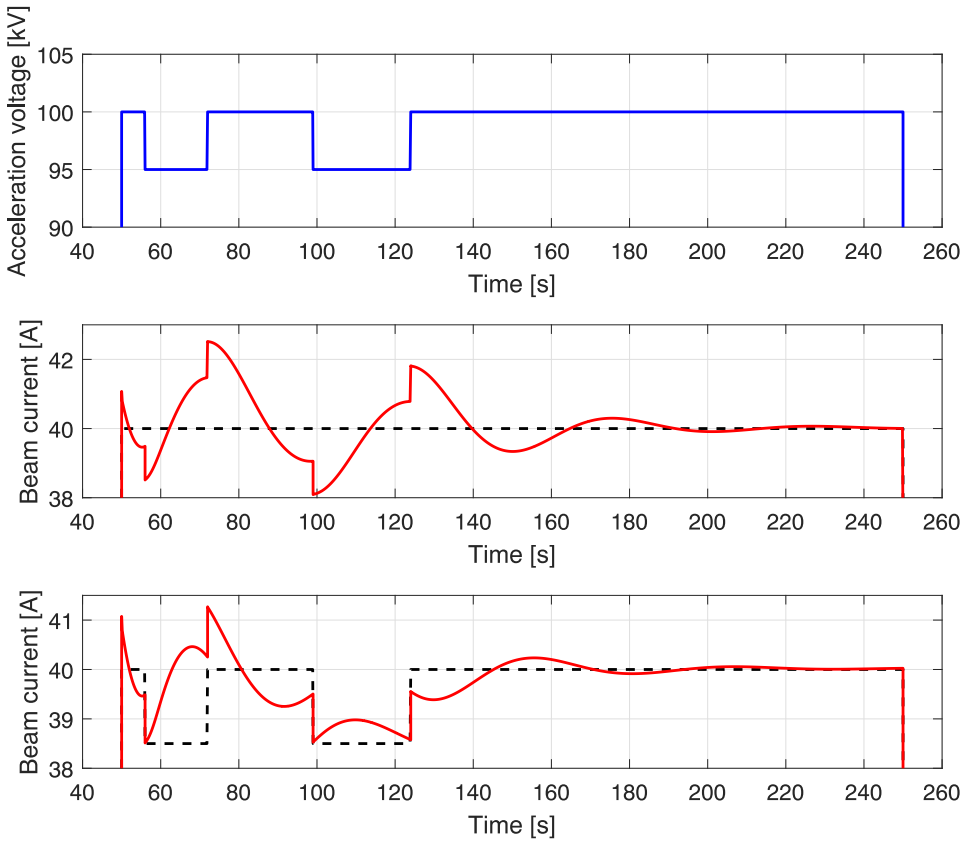


Figure 4.6: The beam current of the control system for a varying acceleration voltage. Top: the varying acceleration voltage. Middle: beam current for constant reference (40A), shows a maximum relative error of 6.3%. Bottom: beam current with a Schottky-varying reference, shows a maximum relative error of 5.1%. The references are indicated by the dashed black lines.

The control system contains an option to either: (1) keep the reference at its fixed value, or (2) allow the reference to vary due to the Schottky barrier lowering, referred to as a Schottky-varying reference. In the second case, when a voltage step is applied, the reference changes with (for high-power pulses):

$$\Delta \text{ref} = 0.3 \Delta V_{\text{acc,kV}}, \quad [\text{A}], \tag{4.3}$$

with $\Delta V_{\text{acc,kV}}$ [kV] the step in acceleration voltage.
The control system is tested at the operating point (40A, 100kV), as this showed the largest relative error in Figure 4.4. As illustrated in the two plots of Figure 4.6, the control system is capable of handling various voltage steps, either for a fixed reference or a Schottky-varying reference. Even more, Figure 4.6 shows the worst-case scenario: here the voltage steps are applied when a peak occurs in the oscillation of the beam current. Specifically, a negative voltage step is applied when the beam current peaks below the reference, and a positive voltage step is applied when the beam current peaks above the reference.

## 4.5 Control system performance: Operating Scenario 3

The last operating scenario in which the control system needs to function, is for a modulated acceleration voltage. The acceleration voltage is modulated from 0kV to a value in the 60-100kV range, with a modulation frequency up to 1kHz. The reference is of course also modulated with the same signal. The duty cycle $D$ of the modulation is assumed to be 0.5.
The control system is not able to operate correctly in this scenario: Design Requirements M3 and M4

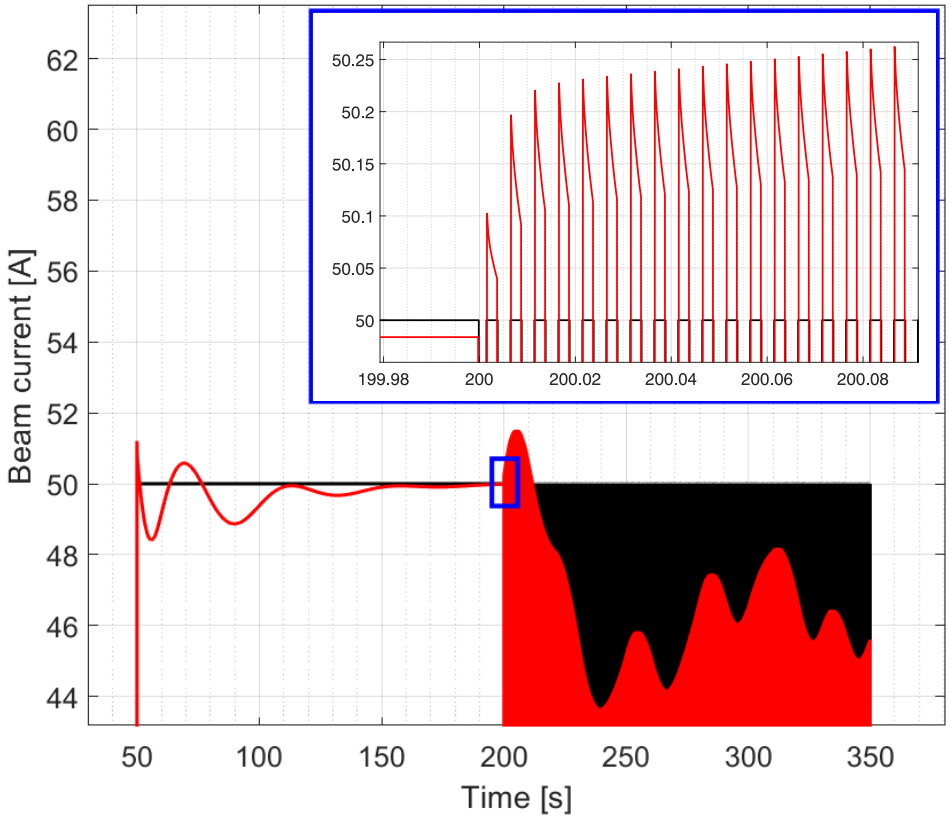


Figure 4.7: The beam current (in red) of the control system for a modulated acceleration voltage. The reference is indicated in black. The blue box shows an enlarged view on the start of the modulation. The signals are modulated from $t = 200$s, in order to show the climbing effect for when the current has (almost) reached a steady-state value. Due to the modulation and the way of drawing, the area under the curves appears to be filled, but the outline of the beam current is still visible. In this example, the reference is 50A, the acceleration voltage is 80kV, the duty cycle of the modulation is 0.5, and the modulation frequency is 100Hz.

are violated, as is shown in the example of Figure 4.7. The reason why becomes clear from the enlarged view at the start of the modulation. Here, the beam current is seen to be "climbing". When the pulse is modulated, the Nottingham effect is cutoff for $(1 - D)$ part of the time, while the heat provided by the filament is the same as in the other scenarios. The result is an accumulation of heat at the emitter, and thus a climbing beam current.

The climbing in itself is bad, as the beam current exceeds the reference. Furthermore, the PI controller reacts too strongly to the first climbing peak (around $t = 210$s in Figure 4.7) and decreases the filament current too much. The result is a completely disrupted control system. This behaviour appears also when the modulation is started at the pulse start.

I try to counter the climbing effect by increasing the duty cycle (leads to more cooling by the Nottingham effect), varying the modulation frequency, changing the PI parameters during modulation, and changing the constraints in the current limiter during modulation. However, none of these attempts stops the climbing. The control system is thus not capable of operating correctly in Operating Scenario 3.

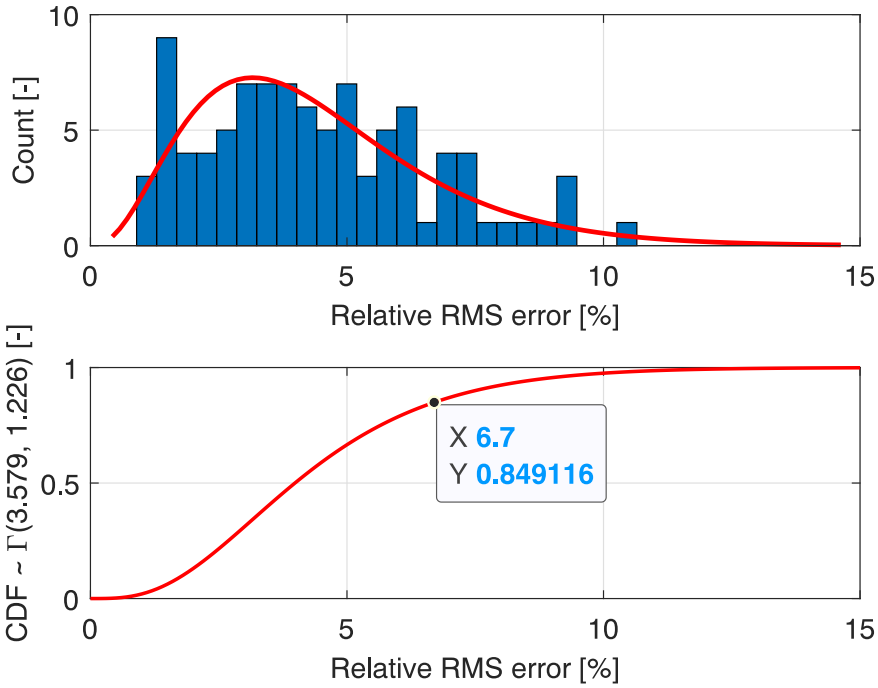


Figure 4.8: Gamma probability distribution for the relative maximum errors of the adapted lumped-element model. Top: histogram of the errors with the fitted Gamma probability density function. Bottom: the associated cumulative distribution function.

## 4.6 Modelling error in the control system

It is important to consider another aspect of the control system: the modelling errors that it contains due to the imperfect MIG model. The MIG model shows significant errors on all test data, as discussed in Section 2.3. Hence, for the real gyrotron, it is not guaranteed that the beam current stays within the 10% reference margin in the entire operating space. In this last subsection, this uncertainty is quantified by lowering the reference margin, and to thus give an operating subspace in which there is a high probability that the control system will satisfy Design Requirement M3.
The relative RMS error $e_{\mathrm{RMS,rel}}$ (for the high-power shots) is considered as a measure of the predictive capabilities of the model. By using the *relative* error, a direct comparison is possible to the reference margin, which is also a relative measure. The relative RMS errors approximately follow a Gamma-(3.579,1.226) probability distribution, as is seen in Figure 4.8. Here is also the cumulative distribution function $F$ plotted, which shows that 85% of the samples[1] have a relative RMS error smaller than 6.7%. Hence, in order to give a more reliable prediction on the operation of the control system in the entire operating space, I change the reference margin from 10% to:

$$\begin{aligned}\text{margin} &= 10\% - F\left(e_{\mathrm{RMS,rel}} < 0.85\right) \\ &= 10\% - 6.7\% = 3.3\%.\end{aligned}$$

The control system is simulated on a uniform 11×11 grid in the operating space, for Operating Scenario 1: a constant reference and acceleration voltage. At each grid point, it is checked if the relative maximum error is smaller than 3.3%.
The result is shown in Figure 4.9. Clearly, the control system does not stay within the lowered margin in the whole operating space: it violates this constraint specifically at the corner points of the operating

[1]The 85% is an arbitrary, but high percentage, here used mainly for illustrating this approach of including the modelling error in the control system's performance analysis.

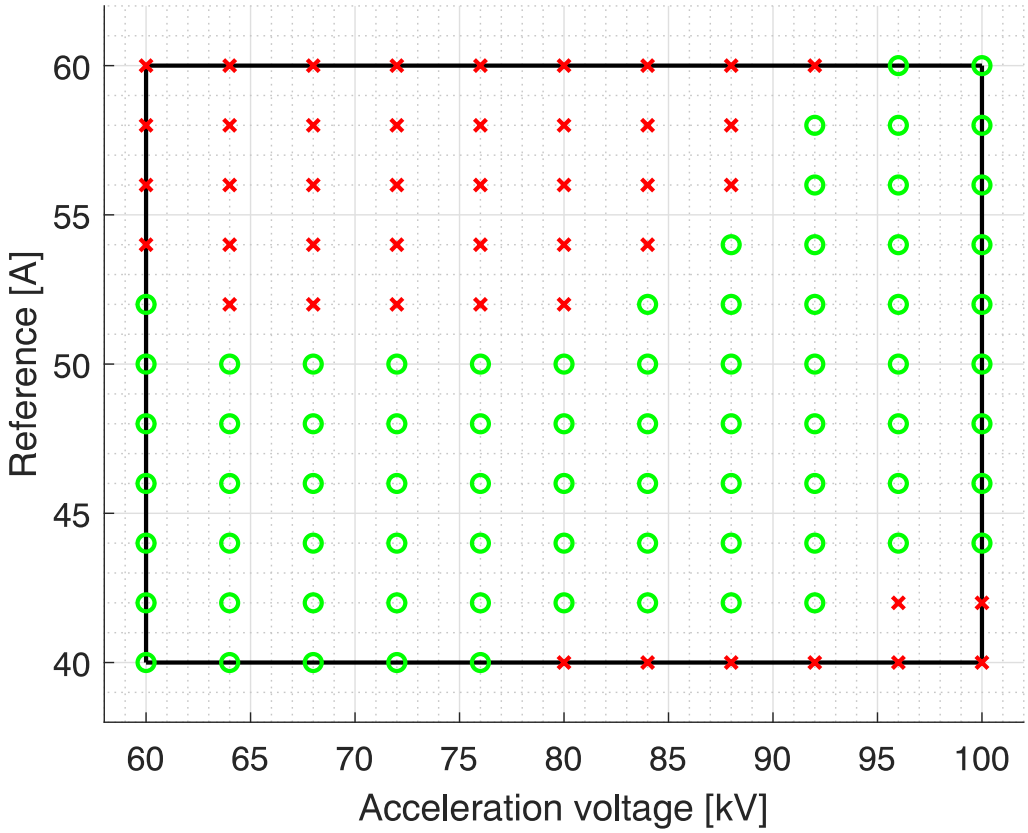


Figure 4.9: The performance of the control system on a uniform 11×11 grid in the operating space. For pulses with a constant reference and acceleration voltage, each sign indicates if the system produces a relative maximum error smaller than 3.3% (green circles) or larger than 3.3% (red crosses).

space, for combinations of a high reference and low voltage, and a low reference and high voltage. These two corners also showed the largest errors in Figure 4.4. On the contrary, the control system stays within the lowered margin in the parts of the operating space where the reference and voltage are both low or both high. From this result, I conclude that -on average- 85% of the shots will stay within the 10%-margin in these parts of the operating space.

# Chapter 5: Conclusion

In this research, a simulated control system was designed that tracks a step-shaped reference of the beam current of the EU ITER gyrotron using the filament current of the MIG as an actuator. First, several significant changes to the original lumped-element MIG model were made to create the adapted lumped-element model. A validated equation was found for the temperature-dependent filament resistance. A new set of view factors was calculated, that ensures conservation of energy. The significant additional power loss due to MIG-external radiation was implemented, including the reabsorption that takes place due to reflections. A new set of tuning parameters was set up, in which all parameters represent physical quantities. The final parameter optimisation proved to be a difficult problem, which could not be solved to satisfaction using a steepest-decent algorithm. In the end, the results of the adapted lumped-element model are *not* good enough to conclude that the model accurately predicts the beam current of the MIG. However, the model could still be used to design the beam-current control system.
Second, besides the lumped-element models, a proof-of-concept was achieved by designing a simple state-space model for low-power pulses. From this work, I conclude that it is possible to construct a black-box model for the MIG, as a non-linear state-space model. Even though that the low-power state-space model is not suitable to use for the design of the control system, it suggests that a similar model can be created for high-power pulses. The difficulty with designing a high-power state-space model, is to find suitable forms for the heating and cooling functions and to optimise their coefficients.
Despite the modelling errors, the lumped-element model proved useful to design the beam-current control system. Using a feedback loop, a feedforward signal, a current limiter, and a controller regulator, the control system is capable of successful operation for pulses with a step-shaped reference and with small additional steps applied to the acceleration voltage. The system is unable to operate with a modulated voltage, and there is no view on an approach that might resolve the issues here. The imperfect model used for the control-system design introduces an uncertainty in the control performance. However, using statistical evidence, I conclude that the system has a high probability to operate correctly in a large part of the operating space. The corners of the operating space in which either the acceleration voltage or the reference is high (but not both) will be the most difficult to operate in with the designed system.
Using this work, the research on the beam-current control system can be continued in two directions simultaneously: the control system can be implemented and tested on the EU ITER gyrotron, and at the same time the MIG models (lumped-element and state-space) can be developed further.

# Chapter 6: Further research

After this study, research remains to be done on the beam-current control system. In this chapter, numerous recommendations are discussed for further research on the MIG models and the beam-current control system.

## 6.1 Control system

Starting with the control system: the most notable action that needs to be taken, is to implement the beam-current control system on the general control system of the TH1509U gyrotron at FALCON. As an initial step towards this, I wrote an outline of the beam-current control algorithm (made available online), and an outline of an experimental plan to test the control system (the next two subsections below). Using this plan, the functionality of the control system can be validated. The plan mainly concerns the case that the control system behaves different than expected. The plan assumes that the beam-current control system has been implemented on the general control system of the TH1509U gyrotron at FALCON. Furthermore, the last subsection gives ideas on how to further develop the control system.

### 6.1.1 Testing for the base case

The first step is to test the control system for the base case of a constant reference of 50A and an acceleration voltage of 80kV for a duration of 200s. The result should look like the middle plot of Figure 4.4. However, it may be that the real system responds differently than the simulated system. Possible discrepancies are:

- The system shows **larger oscillations** than anticipated. The $k_p$ parameter can be decreased to reduce the peak values *above the reference*. However, lowering this parameter worsens the error *below the reference*. If the peak values are also too low below the reference, the feedforward signal must be adjusted. Then the most important parameter to increase is the amplitude of the feedforward during the pulse start, $I_{\mathrm{FF2}}$. The response is quite sensitive to changes in the feedforward. Hence, it is recommended to change the value of $I_{\mathrm{FF2}}$ in steps of 0.2A.
- The system does **not reach a steady-state** in sufficient time. Even though this was no strong requirement in this study, it might be that the system does not reach steady-state in a few hundred seconds. In this case, the $k_i$ parameter must be increased until the result is satisfactory.
- The beam current always **starts below the reference**. In Figure 4.4, the initial value of the beam current was always above the reference. However, if this peak occurs below the reference, either the preheating current $I_{\mathrm{pre}}$ or the first feedforward step $I_{\mathrm{FF1}}$ is too low. Increase the feedforward step if the beam current starts of too low, and then quickly (within 5s) falls even lower. Increase the preheating current if the beam current stays low at the same level for a longer time (more than 5s). Again, it is recommended to change these currents in small steps of 0.2A. The same procedure

applies to the possible case where the beam current starts off too high above the reference, but then the feedforward must be decreased of course.

### 6.1.2 Testing for different operating points

The second step is to try to operate the control system at different operating points. Here, the correction in the feedforward signal is important. Possible discrepancies are:

- The beam current is **too high for low references**, and/or too low for high references. This effect is already apparent in Figure 4.4, but within acceptable margins. The feedforward steps $I_{\mathrm{FF1}}$ and $I_{\mathrm{FF2}}$ need to be adjusted to the reference, as is already done currently. The linear coefficient of $I_{\mathrm{adj}}$ (the factor of 0.06 in Equation (4.2)) can be increased to mitigate the effect as described here (too high beam current for low references, or too low beam current for high references). It can be decreased for the opposite scenario.
- The beam current starts off **too low for low voltages**, and/or too high for high voltages. Also this effect is somewhat visible in Figure 4.4, but still within acceptable margins. If the effect becomes too strong however, a correction to the acceleration voltage should be applied to the feedforward. It is recommended to modify the time duration of the first feedforward step, $t_{\mathrm{FF1}}$, as this value is independent of $I_{\mathrm{adj}}$. This will be convenient if both a current and voltage adjustment need to be made. The time adjustment can be imposed as $t_{\mathrm{adj}} = a(V_{\mathrm{acc}} - (80 + b) \cdot 10^3)$, with $a$ a constant in the order of $0.2{\cdot}10^{-3}$, and $b$ a constant in the order of $\pm 5$. Then, $t_{\mathrm{FF1}} = 7 + t_{\mathrm{adj}}$. It will require some trial-and-error to find values of $a$ and $b$ that give a satisfactory result.

For both the base case and the other operating points, it is very valuable to try creating multiple pulses in a row, with a fixed amount of time between the shots.

### 6.1.3 Further development of the control system

Besides the implementation and testing of the discussed control system, it is useful to further develop it. Some items that may be developed further are in short:

- The control system of this study is not capable yet to operate with a **modulated voltage**. As mentioned in Section 4.5, it is not sufficient to change the duty cycle, the modulation frequency, the PI parameters, or the current limiter constraints. Perhaps there exists a combination of these techniques that does allow the control system to use a modulated voltage. Or, it may be that it is only possible to modulate the voltage in a specific part of the operating space, e.g. only at low references. This requires more research.
- In this research, the **derivative parameter** $k_d$ of the PID controller was set to 0, and the controller was used as PI controller. This was necessary to prevent large spikes in the controller output during a voltage step. It may be possible to schedule the value of $k_d$: to use a nonzero $k_d$ when no voltage step is applied, and briefly set $k_d = 0$ when a voltage step will be applied. This could possibly decrease the oscillations and improve the operation of the control system. Simulations suggest that using a $k_d = 10$ could prevent the oscillations after the initial decrease in beam current at the pulse start. This could decrease the maximum relative error by 0.5 percentage points for low references. However, as shown in Chapter 4, the derivative control is not required, and it was left out for simplicity.
- At the moment, the effect of **arcs** inside the gyrotron is not taken into consideration in the beam-current control system. Experiments show that lower beam currents are realised in the first shot after an arc took place. Hence, for the initial testing of the beam-current control system, should an

arc take place during a shot, the next first shot should be discarded. Once the beam-current control system is operational for regular shots, the effect of arcs can be considered in it (e.g. increase the feedforward for the first shot after an arc).

- At the moment, in the current limiter, the distinction between **a hot and a cold filament** is made simply by looking at the value of the filament current: $I_f \geq 5$A means the filament is hot, and $I_f < 5$A means the filament is cold. However, this distinction is too strict, as it should include some time dependence on how long the filament current has been below 5A. During normal control operation, the filament current will always remain above 5A, and this simplification will thus not give immediate problems.
- Lastly, it is important to mention that the **structure of the control system** can most likely remain the same when the MIG model is developed further. Changes in the model are mainly noticeable at the pulse start. Hence, most likely the only changes that are needed to be implemented are different values for the feedforward signal. The feedforward signal can also be further optimised than was done in this thesis, in order to minimise the errors produced by the control system. This will require more trial-and-error.

## 6.2 Lumped-element model

Regarding the MIG models: I think it is valuable to continue the development of a MIG model. If the goal is to have a model that accurately predicts the thermal dynamics of the MIG and its components, then it is valuable to continue the work on the lumped-element model. If the goal is to have a model that is only used in the beam-current control system, I advise to first put more effort into the black-box modelling, see the next section.
An additional advantage of an accurate lumped-element model is that it could give predictions on new MIG designs: new types or shapes of components can be included in the model, and the effect that these changes have on the beam current can be predicted. Note that for this purpose, the current MIG needs to be modelled very well, including the values of the tuning parameters: these need to provide good results and be physically interpretable. I include some ideas on how to further improve the lumped-element model below. These are as follows:

- As mentioned in the beginning of Chapter 2, the **prolongator and nosecone** are modelled using a uniform dynamic temperature. Their uniform temperature was considered a valid assumption, as this was done for the other components as well. However, the prolongator and nosecone are much larger than the other components. From old simulation results of FengPing Li (postdoc at EPFL in 2014), it appears that the temperature varies by 80-100K over the outside surface of the prolongator and nosecone. A non-uniform temperature on outside surface of the MIG leads to significant changes in the power that is radiated from there (the power loss discussed in Subsection 2.2.3), as $P_{\text{loss}} \propto T^4$. It is very valuable to investigate this non-uniform temperature distribution further, and to implement the prolongator and nosecone in multiple parts (instead of as a single lumped element).
- As described in Subsection 2.2.2, the adapted model's **view factors** are estimated by hand. It is valuable for the model to calculate these accurately, which is possible given an accurate CAD model of the MIG. If this is not possible, it is worthwhile to investigate how sensitive the model's dynamics are to small ($\pm 10\%$) changes in the view factors.
- Besides the components described in this study, the MIG contains **metallic connections**, which keep all components aligned. These connections are not considered in the models, and will provide

heat transfer by conduction and slightly change the view factors. It is valuable to investigate if these connections make a significant change to the model's dynamics.

- The MIG contains an **internal oil-cooling circuit**. The adapted model contains the possibility to model this, by including an additional cooling term at the prolongator. However, the cooling term is linearly proportional to a convective coefficient, which contains a lot of uncertainty. Hence, it was decided to not use this cooling term yet in the model. Most likely, the term is much less significant than other heat losses, as the oil's temperature was experimentally observed to stay almost constant, even during long pulses.
- The physical interpretation of the tuning parameter $f_{\mathrm{A,em}}$ (correction to emitter area) was attributed to the porous material of the emitter, and how the effective area can be slightly different than the measured area. However, it seems that the parameter is also suitable to take into account the uncertainty of the fixed constant in the Richardson-Dushman equation (the factor $120 \cdot 10^4$ in Equation (1.4)). Literature work suggests that in practice the value of this constant can be a factor 0.95 [28, pp.627-638] or even 0.25-0.50 [13, p.44] lower than anticipated.
- For the model's performance, it is very valuable to finish the optimisation problem of the model's **tuning parameters**. The two sets of parameters of Chapter 2 already illustrate how sensitive the model's performance is to small changes in the parameters. It is still not guaranteed that these parameters give the global minimum of the optimisation problem. As discussed in Subsection 2.2.4, the steepest-decent algorithm gets stuck in local minima, and it takes a lot of computational power to try a lot of different initial positions. Hence, it is worthwhile to investigate a different optimisation algorithm, such as a genetic algorithm, or to implement the existing steepest-decent algorithm on a powerful computer.

Besides the development of the model itself, it is worth noting that the adapted model can be used to design new experiments for the gyrotron (without beam-current control system), as the filament resistance is included. In other words, the model can be used to try some inputs on the MIG (e.g. boosting sequences) to see the effect on the beam current.

## 6.3 Black-box model

The simple black-box model of Chapter 3 already shows promising results after a short development time. It could be possible to relatively quickly (compared to improving the lumped-element model) set up a state-space model that provides better results on high-power pulses than the lumped-element models do. This model can then be used to improve the control system of this study: reduce the limitations in the operating space (of Figure 4.9), reduce the maximum errors produced, and reduce the settling time (Design Aspect D1). An additional advantage of this approach is that it could also be applied relatively quickly to design a MIG model for other gyrotrons, which use different MIGs: this approach is better generalisable than the construction of the lumped-element model (Design Aspect D2). There is however no set approach to design a non-linear state-space model. I recommend to try different forms of the heating function $f_1$ used in the low-power model, where this was a linear equation. I suggest to start with a high-order polynomial function for $f_1$, which may better represent the radiative power transfer that goes as $T^4$. I expect that the cooling function $f_2$ can remain a function that goes as $f_2 \propto I_k T_{\mathrm{em}}$, as this is the structure of the power loss due to the Nottingham effect. Last, like for the lumped-element model, I also recommend to try a different algorithm for the optimisation of the state-space model. As the function-evaluation time is considerably shorter than for the lumped-element model, it is valuable to try a second-order algorithm.

# Chapter A: Gyrotron shots

## A.1 High-power shots

The information of the 95 high-power shots used to test the performance of the lumped-element MIG models is summarised in the table below. For each shot, the following is given: the shot number, the acceleration voltage $V_{\text{acc}}$, the filament current before the shot $I_f$, the boosting at the pulse start, and the range of the beam current during the shot $I_k$. All shots are 120s long, unless stated otherwise under "miscellaneous" (misc.). In this last column, an "a" indicates that the shot follows after an arc occurred in the gyrotron.
The boosting is indicated as three steps in filament current, for example for Shot 9635: the filament current has been at 18.2A for a long time before the shot. When the pulse starts, it goes to 21.2A for 0.5s, then to 21.7A for 5s, and then drops to 20.7A for the remainder of the pulse.

Table A.1: High-power shots of gyrotron TH1509U used in this research.

| Shot | $V_{\text{acc}}$ | $I_f$ | Boosting | | | $I_k$ | misc. |
|---|---|---|---|---|---|---|---|
| [-] | [kV] | [A] | [A], [s] | | | [A] | [s] |
| 9635 | 70.0 | 18.2 | 3, 0.5 | 0.5, 5 | -1.0 | 42.9-48.8 | 59 |
| 9669 | 72.0 | 18.3 | 3, 0.5 | 0.5, 5 | -2.0 | 39.9-46.7 | |
| 9680 | 72.5 | 18.4 | 3, 0.6 | 0.5, 5 | -1.4 | 43.5-49.1 | 180 |
| 9682 | 72.5 | 18.4 | 3, 0.7 | 0.5, 5 | -1.4 | 41.4-46.0 | 82 |
| 9722 | 73.5 | 18.5 | 3, 0.8 | 0.5, 7 | -1.3 | 45.2-51.7 | 180 |
| 9734 | 75.0 | 18.6 | 3, 0.8 | 0.5, 7 | -1.3 | 47.0-52.8 | 180, a |
| 9738 | 74.0 | 18.6 | 3, 0.8 | 0.5, 7 | -1.3 | 47.5-53.0 | 180, a |
| 9742 | 75.0 | 18.6 | 3, 0.8 | 0.5, 7 | -1.3 | 47.4-52.8 | a |
| 9752 | 75.0 | 18.6 | 3, 0.8 | 0.5, 7 | -1.3 | 46.8-52.0 | |
| 9756 | 75.0 | 18.6 | 3, 0.8 | 0.5, 7 | -1.3 | 48.2-54.0 | a |
| 9757 | 75.0 | 18.6 | 3, 0.8 | 0.5, 7 | -1.3 | 48.1-53.7 | |
| 9763 | 75.5 | 18.6 | 3, 0.8 | 0.5, 7 | -1.3 | 48.0-53.5 | a |
| 9779 | 74.5 | 18.6 | 3, 0.8 | 0.5, 7 | -1.3 | 42.4-50.0 | a |
| 9781 | 74.5 | 18.6 | 3, 0.8 | 0.5, 7 | -1.3 | 43.9-50.4 | a |
| 9782 | 73.5 | 18.6 | 3, 0.8 | 0.5, 7 | -1.3 | 45.0-50.7 | |
| 9783 | 72.5 | 18.6 | 3, 0.8 | 0.5, 7 | -1.3 | 44.3-50.3 | |
| 9785 | 70.0 | 18.5 | 3, 0.8 | 0.5, 7 | -1.3 | 46.2-51.4 | |
| 9786 | 72.0 | 18.5 | 3, 0.8 | 0.5, 7 | -1.3 | 47.9-54.4 | |
| 9787 | 68.0 | 18.5 | 3, 0.8 | 0.5, 7 | -1.3 | 48.0-55.5 | |
| 9799 | 70.0 | 18.5 | 3, 0.8 | 0.5, 7 | -1.3 | 45.8-51.6 | |
| 9801 | 75.0 | 18.5 | 3, 0.8 | 0.5, 7 | -1.3 | 46.6-52.0 | a |
| 9802 | 76.0 | 18.5 | 3, 0.8 | 0.5, 7 | -1.3 | 47.8-53.6 | |
| 9803 | 77.0 | 18.5 | 3, 0.8 | 0.5, 7 | -1.3 | 47.7-53.5 | |
| 9809 | 77.0 | 18.1 | 3, 0.8 | 0.5, 7 | -1.3 | 43.0-49.4 | |
| 9810 | 78.0 | 18.1 | 3, 0.8 | 0.5, 7 | -1.3 | 42.9-48.9 | |
| 9811 | 80.0 | 18.1 | 3, 0.8 | 0.5, 7 | -1.3 | 43.6-49.2 | |
| 9830 | 78.0 | 18.3 | 3, 0.8 | 0.5, 7 | -1.3 | 44.3-50.4 | |
| 9831 | 80.0 | 18.3 | 3, 0.8 | 0.5, 7 | -1.3 | 45.5-51.7 | |

*Continuation of Table A.1:*

| Shot | $V_{acc}$ | $I_f$ | Boosting | | | $I_k$ | misc. |
|---|---|---|---|---|---|---|---|
| [-] | [kV] | [A] | [A], [s] | | | [A] | [s] |
| 9833 | 82.0 | 18.3 | 3, 0.8 | 0.5, 7 | -1.3 | 43.5-48.3 | a |
| 9837 | 78.0 | 18.3 | 3, 0.8 | 0.5, 7 | -1.3 | 42.7-48.3 | |
| 9838 | 80.0 | 18.3 | 3, 0.8 | 0.5, 7 | -1.3 | 45.6-51.8 | |
| 9839 | 82.0 | 18.3 | 3, 0.8 | 0.5, 7 | -1.3 | 44.9-49.9 | |
| 9841 | 84.0 | 18.3 | 3, 0.8 | 0.5, 7 | -1.3 | 45.9-51.3 | |
| 9852 | 85.0 | 18.3 | 3, 0.8 | 0.5, 7 | -1.3 | 44.6-49.6 | |
| 9855 | 86.0 | 18.3 | 3, 0.8 | 0.5, 7 | -1.3 | 44.6-50.9 | |
| 9857 | 78.0 | 18.3 | 3, 0.8 | 0.5, 7 | -1.3 | 42.8-48.5 | |
| 9858 | 80.0 | 18.3 | 3, 0.8 | 0.5, 7 | -1.3 | 46.8-55.1 | |
| 9861 | 82.0 | 18.3 | 3, 0.8 | 0.5, 7 | -1.3 | 45.2-51.1 | |
| 9879 | 84.0 | 18.3 | 3, 1.0 | 0.5, 7 | -1.3 | 45.8-51.6 | a |
| 9886 | 68.0 | 18.3 | 3, 1.0 | 0.5, 7 | -1.3 | 43.6-49.1 | a |
| 9887 | 70.0 | 18.3 | 3, 1.0 | 0.5, 7 | -1.3 | 43.4-48.7 | |
| 9901 | 72.0 | 18.5 | 3, 1.0 | 0.5, 7 | -1.3 | 48.2-55.0 | |
| 9919 | 72.0 | 18.6 | 3, 1.0 | 0.9, 7 | -1.7 | 49.4-55.7 | |
| 9920 | 74.0 | 18.6 | 3, 1.0 | 0.9, 7 | -1.7 | 49.7-55.3 | |
| 9933 | 75.0 | 18.6 | 3, 1.0 | 0.9, 7 | -1.7 | 48.6-53.8 | |
| 9936 | 76.0 | 18.6 | 3, 1.0 | 0.9, 7 | -1.7 | 49.0-54.4 | |
| 9937 | 72.0 | 18.6 | 3, 1.0 | 0.9, 7 | -1.7 | 47.2-51.9 | |
| 9948 | 74.0 | 18.7 | 3, 1.0 | 0.9, 7 | -1.7 | 49.5-54.9 | a |
| 9970 | 72.0 | 18.6 | 3, 1.0 | 0.9, 7 | -1.7 | 49.8-56.4 | |
| 9973 | 72.0 | 18.6 | 3, 1.0 | 0.9, 7 | -1.7 | 50.1-55.2 | |
| 9979 | 72.0 | 18.6 | 3, 1.0 | 0.9, 7 | -1.7 | 50.3-54.3 | |
| 9986 | 74.0 | 18.6 | 3, 1.0 | 0.9, 7 | -1.7 | 49.6-53.5 | a |
| 9990 | 74.5 | 18.6 | 3, 1.0 | 0.9, 7 | -1.7 | 51.4-55.8 | |
| 9995 | 74.5 | 18.6 | 3, 1.0 | 0.9, 7 | -1.7 | 50.8-55.0 | |
| 9997 | 76.0 | 18.6 | 3, 1.0 | 0.9, 7 | -1.7 | 50.4-54.6 | 103 |
| 10002 | 76.5 | 18.6 | 3, 1.0 | 0.9, 7 | -1.7 | 52.1-56.5 | |
| 10004 | 76.5 | 18.6 | 3, 1.0 | 0.9, 7 | -1.7 | 52.5-56.9 | 119 |
| 10006 | 76.5 | 18.6 | 3, 1.0 | 0.9, 7 | -1.7 | 51.2-55.2 | |
| 10008 | 76.5 | 18.6 | 3, 1.0 | 0.9, 7 | -1.7 | 52.0-56.1 | 101 |
| 10012 | 76.5 | 18.6 | 3, 1.0 | 0.9, 7 | -1.7 | 52.1-56.4 | |
| 10014 | 76.5 | 18.6 | 3, 1.0 | 0.9, 7 | -1.7 | 49.2-56.7 | 256 |
| 10024 | 77.0 | 18.5 | 3, 1.0 | 0.9, 7 | -1.7 | 52.6-57.2 | 178 |
| 10044 | 76.0 | 18.5 | 3, 1.0 | 0.9, 7 | -1.7 | 50.2-55.2 | |
| 10064 | 75.0 | 18.5 | 3, 1.0 | 0.9, 7 | -1.7 | 49.7-53.4 | |
| 10067 | 76.6 | 18.5 | 3, 1.0 | 0.9, 7 | -1.7 | 50.3-55.9 | |
| 10724 | 74.0 | 18.5 | 3, 6.0 | 0.9, 15 | -3 | 39.1-53.1 | 116 |
| 10733 | 74.0 | 18.5 | 3, 6.0 | 0.9, 15 | -2 | 44.6-48.9 | 125 |
| 10734 | 74.0 | 18.5 | 3, 6.0 | 0.9, 15 | -2 | 43.8-47.0 | 203, a |
| 10735 | 74.0 | 18.5 | 3, 6.0 | 0.9, 15 | -2 | 42.5-45.4 | 81 |
| 10736 | 74.0 | 18.5 | 3, 6.0 | 0.9, 15 | -2 | 43.7-46.9 | 152 |
| 10738 | 74.0 | 18.5 | 3, 6.0 | 0.9, 15 | -2 | 42.0-45.0 | 570 |
| 10746 | 74.0 | 18.4 | 3, 6.0 | 0.9, 15 | -2 | 42.2-45.3 | 515 |
| 10753 | 75.0 | 18.6 | 3, 6.0 | 0.9, 15 | -2 | 48.1-54.7 | 256 |
| 10756 | 74.0 | 18.6 | 3, 6.0 | 0.9, 15 | -1.9 | 49.1-53.6 | 538 |
| 10774 | 74.5 | 18.4 | 3, 6.0 | 0.9, 15 | -1.9 | 46.0-51.2 | 612 |
| 10784 | 74.0 | 18.3 | 3, 6.0 | 0.9, 15 | -1.9 | 43.0-46.8 | 397 |
| 10786 | 74.0 | 18.2 | 3, 6.0 | 0.9, 15 | -1.9 | 40.0-45.4 | 684 |
| 10792 | 74.0 | 18.3 | 3, 6.0 | 0.9, 15 | -1.9 | 42.6-45.6 | 940 |
| 10796 | 74.0 | 18.3 | 3, 6.0 | 0.9, 15 | -1.9 | 43.6-48.1 | 1000 |
| 10802 | 74.0 | 18.3 | 3, 6.0 | 0.9, 15 | -1.9 | 42.8-46.2 | |

*Continuation of Table A.1:*

| Shot | $V_{acc}$ | $I_f$ | Boosting | | | $I_k$ | misc. |
|---|---|---|---|---|---|---|---|
| [-] | [kV] | [A] | [A], [s] | | | [A] | [s] |
| 10805 | 74.5 | 18.3 | 3, 6.0 | 0.9, 15 | -1.9 | 43.9-47.9 | |
| 10807 | 74.0 | 18.3 | 3, 6.0 | 0.9, 15 | -1.9 | 42.8-45.9 | |
| 10817 | 74.0 | 18.3 | 3, 6.0 | 0.9, 15 | -1.9 | 43.2-47.5 | |
| 10818 | 74.0 | 18.3 | 3, 6.0 | 0.9, 15 | -1.9 | 42.3-45.4 | |
| 10819 | 74.0 | 18.3 | 3, 6.0 | 0.9, 15 | -1.9 | 42.6-45.4 | |
| 10820 | 74.0 | 18.3 | 3, 6.0 | 0.9, 15 | -1.9 | 42.1-45.2 | |
| 10821 | 74.0 | 18.3 | 3, 6.0 | 0.9, 15 | -1.9 | 42.8-46.1 | |
| 10822 | 74.0 | 18.3 | 3, 6.0 | 0.9, 15 | -1.9 | 44.0-48.0 | |
| 10823 | 74.0 | 18.2 | 3, 6.0 | 0.9, 15 | -1.9 | 39.9-42.6 | |
| 10825 | 74.0 | 18.5 | 3, 6.0 | 0.9, 15 | -1.9 | 45.7-49.4 | |
| 10826 | 74.0 | 18.3 | 3, 6.0 | 0.9, 15 | -1.9 | 39.8-43.0 | |
| 10827 | 72.0 | 18.3 | 3, 6.0 | 0.9, 15 | -1.9 | 39.9-43.1 | |
| 10828 | 70.0 | 18.3 | 3, 6.0 | 0.9, 15 | -1.9 | 40.5-43.5 | |
| 10829 | 68.0 | 18.3 | 3, 6.0 | 0.9, 15 | -1.9 | 40.1-43.6 | |
| 10835 | 74.0 | 18.3 | 3, 6.0 | 0.9, 15 | -1.9 | 42.7-45.9 | |

## A.2 Low-power shots

The information of 44 low-power shots is summarised in the table below. These shots were used to construct the black-box MIG model. For each shot, the following is given: the shot number, the shot duration $t$, the filament current at the start of the shot $I_f$, the filament-current step size which is applied during the shot $I_f$-step, the acceleration voltage $V_{acc}$, the acceleration-voltage step size which is applied during the shot $V_{acc}$-step, and the range of the beam current $I_k$. For some shots, two steps in $V_{acc}$ are given, these are separate steps and do not refer to a step size compared to the initial $V_{acc}$ value.

Table A.2: Low-power shots of gyrotron TH1509U used in this research.

| Shot | $t$ | $I_f$ | $I_f$-step | $V_{acc}$ | $V_{acc}$-step | $I_k$ |
|---|---|---|---|---|---|---|
| [-] | [s] | [A] | [A] | [kV] | [kV] | [A] |
| 11065 | 600 | 16.5 | 3.0 | 19.6 | 0.0 | 8.6-25.0 |
| 11074 | 600 | 16.5 | 3.0 | 19.9 | 0.0 | 8.3-24.8 |
| 11078 | 600 | 17.6 | 1.0 | 19.5 | 0.0 | 14.4-20.4 |
| 11084 | 1000 | 17.5 | -1.0 | 32 | 0.0 | 9.0-23.4 |
| 11086 | 1200 | 17.5 | 0.0 | 21.6 | 0.0 | 12.3-18.4 |
| 11087 | 1000 | 17.0 | 1.0 | 32.3 | 0.0 | 12.2-16.8 |
| 11090 | 1000 | 17.0 | 0.5 | 32.3 | 0.0 | 12.1-15.5 |
| 11092 | 1000 | 16.6 | 1.0 | 32.3 | 0.0 | 10.6-15.3 |
| 11093 | 1000 | 17.6 | 0.5 | 32.3 | 0.0 | 16.1-25.0 |
| 11094 | 1000 | 16.5 | 0.5 | 32.3 | 0.0 | 10.6-14.6 |
| 11095 | 1000 | 16.5 | 1.0 | 32.3 | 0.0 | 10.2-14.3 |
| 11096 | 1000 | 17.0 | 0.5 | 32.3 | 0.0 | 12.7-16.6 |
| 11100 | 10 | 17.0 | 0.0 | 22.2 | 2, 8 | 14.1-16.0 |
| 11101 | 10 | 17.0 | 0.0 | 22.2 | 2, 8 | 13.9-15.7 |
| 11102 | 10 | 17.0 | 0.0 | 22.2 | 10 | 13.1-15.7 |
| 11103 | 10 | 17.0 | 0.0 | 22.2 | 10 | 13.0-15.6 |
| 11104 | 10 | 17.0 | 0.0 | 22.2 | 10 | 12.8-15.4 |
| 11108 | 10 | 16.5 | 0.0 | 22.2 | 10 | 10.1-11.8 |
| 11109 | 10 | 16.5 | 0.0 | 22.2 | 10 | 10.0-11.8 |
| 11110 | 10 | 16.5 | 0.0 | 22.2 | 10 | 10.0-11.7 |
| 11111 | 10 | 16.5 | 0.0 | 22.2 | 2, 8 | 10.4-11.9 |
| 11112 | 10 | 16.5 | 0.0 | 22.2 | 2, 8 | 10.3-11.7 |

*Continuation of Table A.1:*

Table A.3: Low-power shots of gyrotron TH1509U used in this research.

| Shot | $t$ | $I_f$ | $I_f$-step | $V_{\mathrm{acc}}$ | $V_{\mathrm{acc}}$-step | $I_k$ |
|---|---|---|---|---|---|---|
| [-] | [s] | [A] | [A] | [kV] | [kV] | [A] |
| 11113 | 10 | 15.0 | 0.0 | 22.2 | 2, 8 | 4.7-5.4 |
| 11114 | 10 | 15.0 | 0.0 | 22.2 | 2, 8 | 4.5-5.2 |
| 11115 | 10 | 15.0 | 0.0 | 22.2 | 2, 8 | 4.3-5.0 |
| 11116 | 10 | 15.0 | 0.0 | 22.2 | 10 | 4.1-4.7 |
| 11117 | 10 | 15.0 | 0.0 | 22.2 | 10 | 4.0-4.6 |
| 11118 | 10 | 15.5 | 0.0 | 22.2 | 10 | 5.0-5.9 |
| 11119 | 10 | 15.5 | 0.0 | 22.2 | 10 | 5.1-5.9 |
| 11120 | 10 | 15.5 | 0.0 | 22.2 | 2, 8 | 5.2-6.0 |
| 11121 | 10 | 15.5 | 0.0 | 22.2 | 2, 8 | 5.2-6.0 |
| 11122 | 10 | 16.0 | 0.0 | 22.2 | 2, 8 | 7.5-8.5 |
| 11123 | 10 | 16.0 | 0.0 | 22.2 | 2, 8 | 7.5-8.5 |
| 11124 | 10 | 16.0 | 0.0 | 22.2 | 10 | 7.4-8.7 |
| 11125 | 10 | 16.0 | 0.0 | 22.2 | 10 | 7.4-8.7 |
| 11127 | 10 | 17.6 | 0.0 | 22.2 | 10 | 19.1-23.2 |
| 11128 | 10 | 17.6 | 0.0 | 22.2 | 10 | 18.3-22.4 |
| 11129 | 10 | 17.6 | 0.0 | 22.2 | 2, 8 | 18.7-21.2 |
| 11130 | 10 | 17.6 | 0.0 | 22.2 | 2, 8 | 18.3-20.8 |
| 11131 | 1200 | 17.6 | 0.0 | 22.0 | 0.0 | 12.9-19.1 |
| 11132 | 1150 | 17.0 | 0.0 | 22.0 | 0.0 | 10.1-15.5 |
| 11133 | 1150 | 16.5 | 0.0 | 22.0 | 0.0 | 7.8-11.5 |
| 11134 | 1000 | 16.5 | 2.0 | 32.3 | 0.0 | 9.5-20.5 |
| 11135 | 1000 | 17.5 | -2.0 | 32.0 | 0.0 | 5.8-13.9 |

# Bibliography


[1] J. Freidberg, *Plasma Physics and Fusion Energy*. Cambridge University Press, 2007.

[2] International Energy Agency, "Data and statistics: Explore energy data by category, indicator, country or region: Balances, World, 2019," 2021, Last accessed on 2 June 2022. [Online]. Available: https://www.iea.org/data-and-statistics/data-browser?country=WORLD&fuel=Energy%20supply&indicator=TESbySource

[3] Fusion for Energy, "Consolidated Annual Activity Report (CAAR) for 2020 of the European Joint Undertaking for ITER and the Development of Fusion Energy," 2020, Last accessed on 2 June 2022. [Online]. Available: https://fusionforenergy.europa.eu/wp-content/uploads/2021/07/CAAR_-2020_-Final-Version-WEB-1.pdf

[4] N. Lopes Cardozo, A. Lange, G. Kramer, "Fusion: Expensive and Taking Forever?" *Journal of Fusion Energy*, vol. 35, pp. 94–101, 2016.

[5] M. Thumm, G. Denisov, K. Sakamoto, and M. Tran, "High-power gyrotrons for electron cyclotron heating and current drive," *Nuclear Fusion*, vol. 59, 073001, 2019.

[6] F. Chen, *Introduction to Plasma Physics and Controlled Fusion: third edition*. Springer International Publishing Switzerland, 2016.

[7] J.-P. Hogge, "Fusion and Industrial Plasma Technologies: Millimeter Wave Systems: Part 2: High Power: The gyrotron," 2021, Lecture given at EPFL.

[8] ITER Organization, "External Heating Systems," no date, Last accessed on 9 June 2022. [Online]. Available: https://www.iter.org/mach/Heating

[9] ——, "ITER Technology: the year of the gyrotron," 2018, Last accessed on 14 June 2022. [Online]. Available: https://www.iter.org/newsline/-/2931

[10] M. Henderson, G. Saibene, C. Darbos, D. Farina, L. Figini, M. Gagliardi, F. Gandini, T. Gassmann, G. Hanson, A. Loarte, T. Omori, E. Poli, D. Purohit, and K. Takahashi, "The targeted heating and current drive applications for the ITER electron cyclotron system," *Physics of Plasmas*, vol. 22, 021808, 2015.

[11] ITER Organization, "ITER - the way to new energy," 2022, Last accessed on 14 June 2022. [Online]. Available: https://www.iter.org/

[12] Z. Ioannidis, F. Albajar, S. Alberti, K. Avramidis, W. Bin, T. Bonicelli, A. Bruschi, J. Chelis, F. Fanale, G. Gantenbein, J. Genoud, J.-P. Hogge, V. Hermann, S. Illy, J. Jelonnek, J. Jin, W. Kasparek, G. Latsase, F. Legrand, C. Lechte, I. Pagonakis, T. Rzesnicki, F. Sánchez, C. Schlatter, M. Schmid, I. Tigelis, M. Thumm, M. Tran, A. Zisis, A. Zein, "Recent experiments with the European 1MW, 170GHz industrial CW and short-pulse gyrotrons for ITER," *Fusion Engineering and Design*, vol. 146, pp. 349–352, 2019.

[13] A. Gilmour, Jr., *Klystrons, Traveling Wave Tubes, Magnetrons, Crossed-Field Amplifiers, and Gyrotrons*. Artech House, 2011.

[14] N. Badodi, A. Cammi, A. Leggieri, F. Sanchez, and L. Savoldi, "A New Lumped Approach for the Simulation of the Magnetron Injection Gun for MegaWatt-Class EU Gyrotrons," *Energies*, vol. 14, 2068, 2021.

[15] W. Nottingham, "Remarks on Energy Losses Attending Thermionic Emission of Electrons from Metals," *Physical Review*, vol. 59, pp. 906–907, 1940.

[16] F. Charbonnier, R. Strayer, L. Swanson, E. Martin, "Nottingham Effect in Field and T-I Emission: Heating and Cooling Domains, and Inversion Temperature," *Physical Review Letters*, vol. 13, pp. 397–401, 1964.

[17] R. Bertazzoni, "A physics-based model of the EU 1MW 170GHz Gyrotron's MIG for control system design," 2022, M.S. thesis, Politecnico Milano. [Online]. Available: https://www.politesi.polimi.it/handle/10589/197033

[18] G. Witvoet, "4CM00: Control Engineering: Stability," 2016, Lecture slides.

[19] F. Felici, "School on Control and Operation of Tokamaks: General Intro & Basic Control Recap," 2023, Presentation given on 6 February 2023 at EPFL, Switzerland.

[20] D. Fasel, S. Alberti, J. Dubray, T. Goodman, J.-P. Hogge, D. Minelli, U. Siravo, A. Perez, F. Albajar, G. Carannante, P. Sanchez, F. Sartori, M. Cavinato, L. De Frutos, "Enhanced operation of the Eu Ec test facility," *Fusion Engineering and Design*, vol. 146, pp. 1942–1946, 2019.

[21] H. Bernstein, *Measuring electronics and sensors : basics of measurement technology, sensors, analog and digital signal processing*. Springer, 2022.

[22] F. Incropera, D. DeWitt, T. Bergman, A. Lavine, *Fundamentals of heat and mass transfer: sixth edition*. John Wiley & Sons, 2007.

[23] W. Coblentz, "The reflecting power of various metals," 1910, Last accessed on 20 October 2022. [Online]. Available: www.nvlpubs.nist.gov/nistpubs/bulletin/07/nbsbulletinv7n2p197_A2b.pdf

[24] R. Powell, C. Ho, P. Liley, *Thermal conductivity of selected materials*. U.S. Department of Commerce, National Bureau of Standards, 1966, 1966.

[25] M. Hochstenbach, "2DME20/2MMD10 Optimization: Numerical continuous unconstrained optimization," 2021, Lecture given at Eindhoven University of Technology.

[26] L. Wang, *PID Control System Design and Automatic Tuning using MATLAB/Simulink*. John Wiley & Sons Ltd, 2020.

[27] K. Åström, T. Hägglund, "Revisiting the Ziegler–Nichols step response method for PID control," *Journal of Process Control*, vol. 14, pp. 635–650, 2004.

[28] F. Huffman, *Encyclopedia of Physical Science and Technology: third edition*. Thermionic energy conversion. Ramtech, Inc., Tarzana, California, USA, 2001.

# Acknowledgements

At the end of this graduation project, I thank Tom Huiskamp and Roger Jaspers for supervising this double-degree project and for their advice during it. I thank Jean-Philippe Hogge, Stefano Alberti, and Timothy Goodman for supervising this project, for all our interesting discussions on the project and gyrotrons, and for welcoming me to the SPC multiple times. I thank Andrea Antonione and Ruggero Bertazzoni for the very nice collaboration on the development of the lumped-element MIG model. I thank Jérémy Genoud for the help with the experiments and setting up the dataflow. I thank Jesse Koenders for his explanations on the basics of system identification and control stability. I thank Roy Bakker for the many questions about my project, which forced me to look for a better understanding of many things. Last, I thank Stichting 3E for providing financial aid during my time in Switzerland.

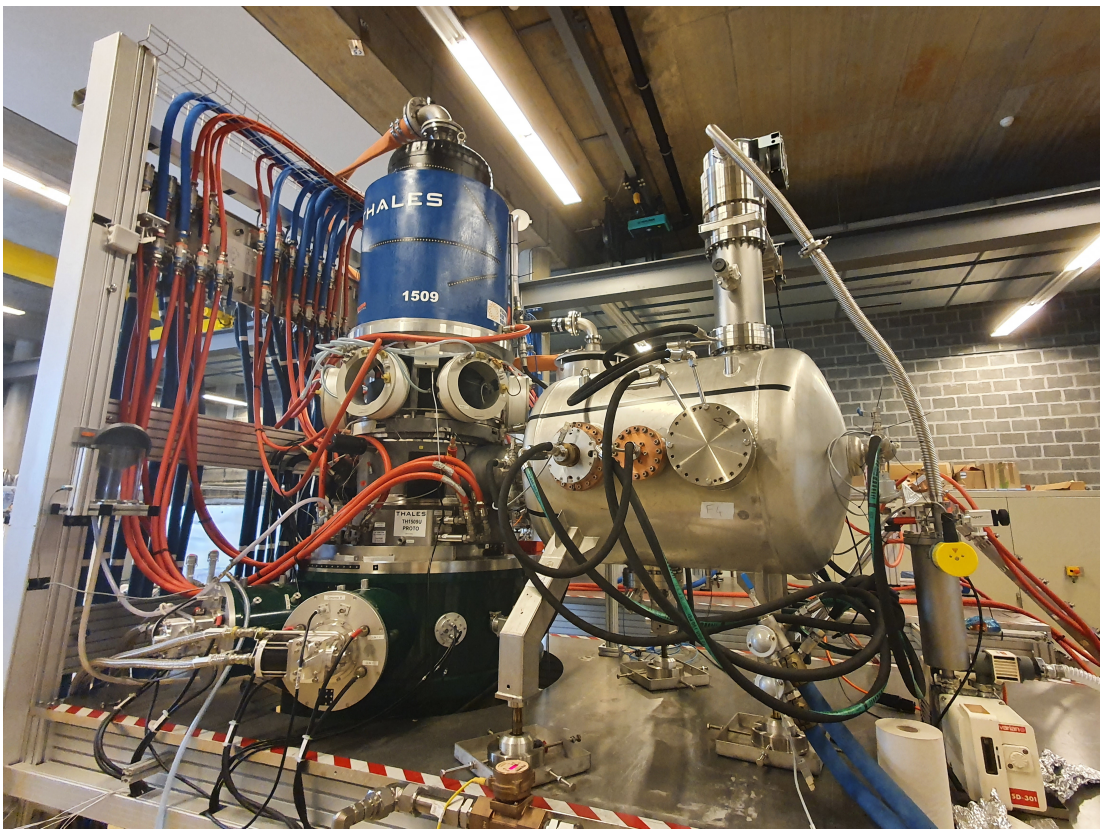


The EU ITER Gyrotron at the FALCON test stand at the Swiss Plasma Centre, Lausanne, Switzerland.